LA-UR-14-27758
Approved for public release; distribution is unlimited.

Title: FY14.CASL.012, L2:MPO.P9.03 Demonstration of Atomistically--informed Multiscale Zr Alloy Deformation Models in Peregrine for Normal and Accident Scenarios

Author(s): Stanek, Christopher Richard
Tome, Carlos
Montgomery, Robert
Liu, Wengfeng

Intended for: Report

Issued: 2014-10-06

CASL-U-2014-201-000

Power uprates
and plant life extension

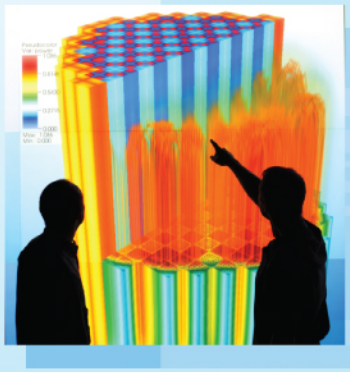

Engineering design
and analysis

Science-enabling
high performance
computing

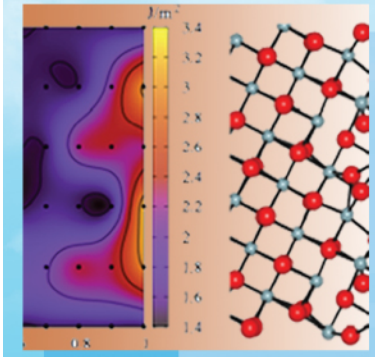

Fundamental science

Plant operational data

Consortium for Advanced Simulation of LWRs

FY14.CASL.012

L2:MPO.P9.03

Demonstration of Atomistically-informed Multiscale Zr Alloy Deformation Models in Peregrine for Normal and Accident Scenarios

Wengfeng Liu
(ANATECH Corp.)
Robert Montgomery
(Pacific Northwest National Laboratory)
Chris Stanek and Carlos Tomé
(Los Alamos National Laboratory)

September 30, 2014

U.S. DEPARTMENT OF ENERGY | Nuclear Energy

REVISION LOG

Revision	Date	Affected Pages	Revision Description

Document pages that are:

Export Controlled _____

IP/Proprietary/NDA Controlled_____

Sensitive Controlled_____

Requested Distribution:

To:

Copy:

EXECUTIVE SUMMARY

Accurate prediction of cladding mechanical behavior is a key aspect of modeling nuclear fuel behavior. This is especially true for the CASL challenge problems: pellet-cladding interaction (PCI), reactivity-initiated accidents (RIA), and loss of coolant accidents (LOCA). Current approaches to fuel performance modeling rely on empirical models for cladding creep, growth and plastic deformation, which are limited to the materials and conditions for which the models were developed. CASL has endeavored to improve upon this approach by incorporating a microstructurally-based, atomistically-informed, zirconium alloy mechanical deformation analysis capability into the Peregrine engineering scale fuel performance code. Specifically, the viscoplastic self-consistent (VPSC) polycrystal plasticity modeling approach, developed by Lebensohn and Tomé (1993), has been implemented in to Peregrine, and has the ability to represent the mechanistic material processes controlling the deformation behavior of the cladding, such as dislocation glide and climb, dislocation-dislocation interactions, and dislocation vacancy/interstitial interactions. A critical component of VPSC is the representation of the crystallographic orientation of the grains within the matrix material and the ability to account for the role of texture on deformation. These capabilities far exceed the functionality of typical semi-empirical constitutive models employed in fuel behavior codes to model irradiation growth and creep, thermal creep, or plasticity. This report describes the implementation of VPSC in to Peregrine and provides initial results utilizing the coupled functionality.

This report consists of an introductory paragraph that describes cladding deformation mechanisms in LWR fuel and the limitations of the current empirical models of cladding behavior. Section 2 provides a primer for the VPSC code, and an overview of its capabilities that offer significant advantages over current approaches. Section 3 provides details of the software interface between the Peregrine and VPSC codes. Finally, Section 4 provides results of Peregrine using the coupled VPSC capability. In the process of performing this work, additional tasks to further refine the important capability that has been established have been identified and are summarized in Section 5.

CONTENTS

FIGURES

TABLES

1. INTRODUCTION

The US DOE's Consortium for Advanced Simulation of Light Water Reactors (CASL) program is developing multiphysics, multi-dimensional modeling and analysis capabilities to assess safety margins and the impact of plant operation on fuel rod behavior. Integral to this endeavor is the research and development activities to expand mechanistic material behavior modeling that builds on the recent advances in computational material science, such as ab-initio calculations using density functional theory to determine certain diffusion/interaction rate constants or microstructurally-aware crystal plasticity methods to represent dislocation behavior within individual grains. Significant improvements are possible in fuel performance modeling and analysis provided that expanded microscale models of the underlying physics controlling material behavior can implemented.

The processes that control the behavior of fuel and cladding materials consist of a complex interaction between pre-existing material microstructural features and the changes caused by the imposed thermal, mechanical, chemical, and irradiation conditions. Traditional fuel behavior modeling capabilities are built on a suite of empirical or semi-empirical material property or behavior models. These models have been derived from a variety of testing and characterization programs that contained limited sets of environmental conditions or material characteristics. While fuel and cladding material behavior under irradiation conditions are among the most complex physics to simulate and understand, there are many areas where improved mechanistic modeling can have significant impact in the realm of fuel behavior simulation and analysis. These areas include the diffusion of fission gas atoms in UO_2 ceramic material, evolution of UO_2 thermal conductivity under irradiation, and zirconium alloy deformation mechanisms resulting from fast neutron damage.

This report provides an overview of the activities to incorporate a microstructurally-based, atomistically-informed, zirconium alloy mechanical deformation analysis capability into the Peregrine engineering scale fuel performance code. The viscoplastic self-consistent (VPSC) polycrystal plasticity modeling approach, developed by Lebensohn and Tomé (1993), has the ability to represent the mechanistic material processes controlling the deformation behavior of the cladding, such as dislocation glide and climb, dislocation-dislocation interactions, and dislocation vacancy/interstitial interactions. A critical component of VPSC is the representation of the crystallographic orientation of the grains within the matrix material and the ability to account for the role of texture on deformation. These capabilities far exceed the functionality of typical semi-empirical constitutive models employed in fuel behavior codes to model irradiation growth and creep, thermal creep, or plasticity. While the empirical models for zirconium alloy creep, growth, and plasticity have been used over the years with large data sets for validation, limitations remain when changes are made to: the material fabrication process, alloy composition, the operational demand envelop to regimes of higher fast fluence, elevated temperatures, or increased applied stress. The use of a Zr-alloy constitutive model that is based on a mechanistic understanding of the microstructural characteristics can allow for extension of fuel performance modeling to applications of improved cladding materials or new operating regimes where validation data is limited.

The structure of the report is as follows. Section 1 provides an overview of the current methods used to model cladding deformation during irradiation in the Peregrine fuel performance tool. The empirical material models used in Peregrine and their limitations are briefly discussed along with a description of the vision to incorporate VPSC. Section 2 summarizes the theoretical bases and approaches used in VPSC to model the anisotropic deformation behavior of hexagonal-closed packed materials such as zirconium alloy cladding tubes. This section includes an overview of the

dislocation motion and interaction mechanisms included in VPSC to represent irradiation-induced creep and growth. Section 3 describes the approach used to interface VPSC with Peregrine and the results from the verification exercises to demonstrate the MOOSE-based interface is working as expected. A series of demonstration analyses using the Peregrine-VPSC interface is summarized in Section 4. Two different demonstration cases are presented; irradiation growth calculations for a set of non-fueled rods irradiated as part of an EPRI program and a high temperature thermal creep case that has been prepared in support of LOCA analysis preparations. These demonstration cases highlight the advantages and features of using a mechanistic material constitutive material modeling on the cladding deformation behavior. Section 5 summarizes the accomplishments to date and provides a roadmap to developing a more complete implementation of a microstructurally-aware, atomistically-informed zirconium alloy cladding constitutive model for irradiation and stress induced deformations during normal operation and transient events in a LWR.

1.1 Cladding Mechanical Behavior in LWRs

The fuel cladding is the first barrier in the reactor to prevent the release of radioactive fission products and actinides into the environment. In LWRs, the cladding tube is generally fabricated from zirconium alloy materials that are ~98% zirconium and 2% alloying elements or impurities (such as iron, nickel, chromium, tin, and niobium). Knowledge of the thermal, mechanical, and chemical properties of the zirconium-alloy cladding for LWR fuels is very important to the safe and economic operation of nuclear reactors. In particular, understanding the mechanical strength change of zirconium-alloys for in-reactor conditions and the deformation behavior of zirconium-alloy cladding tubes under normal operation and accident conditions are of great value to the improvement of fuel performance and to the prevention of fuel rod failures.

Zirconium and zirconium-alloys crystallize in a hexagonal closed-packed (HCP) crystallographic structure at temperatures corresponding to normal operation in LWRs. The material undergoes a phase transition to a body centered cubic (BCC) structure at temperatures above 750-850°C, depending on the alloy composition. As with other HCP materials, zirconium alloys exhibit anisotropic mechanical behavior that is a function of the fabrication process. The thermo-mechanical processing variables result in a crystallographic texture that is important, both in the throughput in the fabrication process (ease of forming) and for the in-reactor mechanical behavior. The zirconium-alloy tube texture impacts the irradiation growth, thermal and irradiation creep, yield strength, and the anisotropy of plastic deformation. It is therefore important to capture the role of as-fabricated texture and irradiation damage on texture evolution in the material constitutive models used to calculate the performance of fuel cladding during normal operation and accident conditions.

The in-reactor deformation of zirconium-alloy materials consists of thermal expansion, elastic strain, irradiation growth, thermal and irradiation creep, and instantaneous plastic strain. The thermal expansion and elastic strain behavior are relatively well understood and are functions of temperature, oxygen content, and texture. The elastic modulus also has a limited dependence on fast neutron fluence. *The primary areas of concern for understanding and predicting the irradiation performed of LWR fuel are:* ***irradiation growth, irradiation and thermal creep, and plastic deformation.*** Irradiation growth refers to the cladding tube elongation in the axial direction caused by the accumulation of irradiation damage. Even though irradiation growth can cause small changes (a few millimeters in the full length fuel rod at the end of life), the differential growth may lead to fuel rod bowing, rod to rod or rod to nozzle contact, and the potential for fuel rod failure. The in-reactor creep of zirconium-alloy cladding is a time-dependent deformation process under relatively lower stress (as compared to the yield strength). Creep deformation is composed of two components, thermal creep and irradiation-induced creep. These processes are complex functions of temperature,

irradiation damage, and stress. Irradiation complicates the creep processes by creating mobile dislocations that promote creep deformation and by retarding the thermal creep through interaction between irradiation defects and dislocations. The creepdown of the cladding tube under the high coolant pressure at the beginning of life could, in combination with the pellet expansion and swelling, reduce and close the fuel-clad gap, thus affecting the fuel temperature and increasing the potential for high cladding tensile stress during a power increase. Under fast power ramps, thermal creep can relax the stress applied on the cladding tube from pellet-clad mechanical contact. Stress relaxation is an important component of the processes that reduce the cladding failure potential during power maneuvers. Plant operators use empirical operating strategies that include constant power hold periods to promote cladding stress relaxation, to mitigate the consequences of pellet-cladding interaction (PCI). In postulated accident conditions, the mechanical deformation of the cladding can be large due to either high temperature or high stress. The non-recoverable deformation caused by either creep or instantaneous plasticity becomes important for accident conditions because these deformations can affect the core coolable geometry or lead to ductile rupture or brittle fracture of the cladding.

During normal operation, persistent changes in the microstructure, chemistry, and geometry of the pellet and cladding occur in response to thermal processes, chemical reactions, fission or irradiation damage, and mechanical forces. These changes can have an important impact on the behavior of a fuel rod during normal operation such as undesired geometry changes, material wastage or embrittlement. Additionally, the evolution of the material properties can impact the fuel rod response to rapid changes in environmental conditions, such as an increase in power to follow electric grid energy demands or a reactor system accident leading to rapid power increase (e.g. RIA) or loss of fuel rod cooling (e.g. LOCA).

An example of the role of irradiation-induced material property changes on fuel rod behavior is shown schematically in Figure 1-1 as a function of burnup. Figure 1-1 depicts the changes in pellet-cladding gap thickness with irradiation caused by pellet relocation, pellet swelling, and cladding creep and the decrease of the cladding ductility induced by outer surface corrosion and hydrogen absorption effects (Montgomery et al, 2004). Simulation of the processes leading to cladding failure during normal operation (e.g. PCI) and during transient conditions (e.g. RIA and LOCA) requires a modeling approach that considers the coupled thermo-mechanical-chemical behavior on-going in a fuel rod during the operating life-time, operational transients, and accident events.

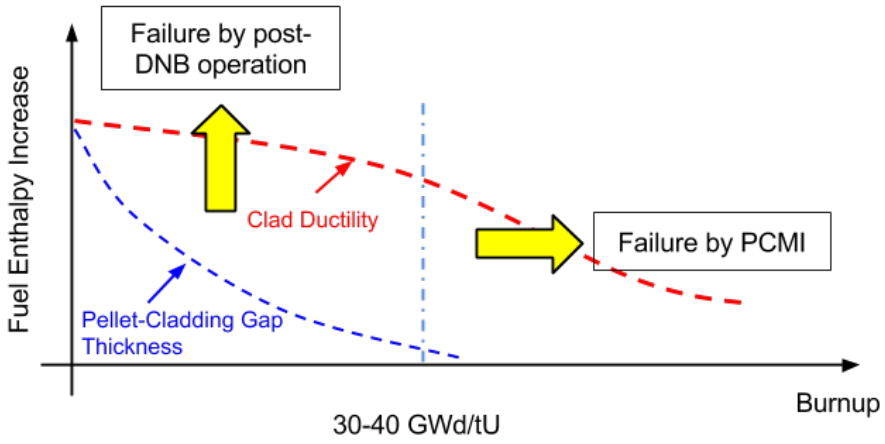

Figure 1-1 Evolution of RIA fuel failure mechanisms as a function burnup, and impact on key fuel rod characteristics (Montgomery, 2003)

The importance of accounting for changes in fuel rod behavior due to irradiation has been demonstrated by RIA and LOCA fuel testing on highly irradiated fuel rods over the last twenty years. Some examples of irradiation-induced cladding material property changes that impact fuel behavior include; 1) irradiation-induced creep and growth leading to cladding creepdown, pellet-cladding contact, and tensile stresses during power increases, 2), cladding corrosion during operation can result in hydrogen pickup into the cladding and the formation of zirconium hydrides that, when combined with irradiation-induced damage embrittlement of the cladding and 3) the presence of hydrogen enhances oxygen diffusion and changes in oxygen solubility during high temperature oxidation and material embrittlement following thermal quench.

1.2 Current Modeling Approach And Limitations

Current fuel performance codes model the deformation of cladding tube as a mechanical equilibrium problem using either a thin-shell theory or using finite element method. Both approaches require a constitutive law to describe the material response under different types of deformation mechanisms, including thermal expansion, elastic deformation, thermal and irradiation-induced creep, irradiation growth, and instantaneous plasticity. Most constitutive models assume that these mechanical deformation processes are additive, and under input variables of temperature, irradiation dose (fast neutron flux), stress, a set of empirical equations are used to describe the contribution of the different deformation mechanisms.

Below is an overview of the three most important cladding deformation mechanisms modeled in fuel performance codes; thermal and irradiation creep, irradiation growth, and plastic deformation (in the case of transient events). The empirical models currently used in Peregrine are used to highlight typical dependencies on temperature, material characteristics (cold-work), stress, and irradiation damage. The literature contains many other empirical or semi-empirical cladding constitutive models.

Thermal and Irradiation Creep

In-reactor creep involves several mechanisms, including thermal creep and irradiation-induced creep. The complex nature of the HCP microstructure in zirconium alloys has important implications on the creep behavior. The thermal creep of zirconium alloys has been studied extensively as it is relatively easy to conduct measurements on the thermal creep. Zirconium alloys exhibit a power law-like thermal creep behavior with complex dependencies on texture, alloy elements, and stress level. Experimental results suggest that diffusional processes (dislocation climb) primarily control the thermal creep rate. In a radiation environment, creep mechanisms become much more complicated. Defect clusters in zirconium-alloys can assist creep deformation in addition to thermal creep. Irradiation can also have hardening effects, which tend to reduce the thermal creep rate. At the initial loading or change of loading, a rapid creep deformation, primary creep, can occur until it finally settles into a steady state. Those mechanisms generally need to be included in the creep equations, which combine the primary (transient) creep and secondary (steady-state) creep including thermal and irradiation creep for modeling fuel rod response. Empirical fitting parameters are used in the creep laws to best represent the data in its applicable ranges. In the traditional fuel codes such as FRAPCON (Geelhood, 2011) and Falcon (Rashid, 2004), Limbäck creep model (Limbäck, 1996) has been used to compute in-reactor creep of fuel cladding.

Limbäck creep model describes several mechanisms of in-reactor creep of zirconium cladding tube. The steady state creep rates are described in the following equations:

$$\dot{\varepsilon}_{th} = A\frac{E}{T}\left(\sinh\frac{a_i\sigma_{eff}}{E}\right)^n \exp\left(-\frac{Q}{RT}\right) \quad (1\text{-}1)$$

$$\varepsilon_i = C_0\phi^{C_1}\sigma_{eff}^{C_2} \quad (1\text{-}2)$$

$$\varepsilon_p = \varepsilon_p^s[1-\exp(-C\sqrt{\dot{\varepsilon}_s t})] \quad (1\text{-}3)$$

Where,

$\dot{\varepsilon}_{th}$ is secondary thermal creep rate (hr^{-1})

$\dot{\varepsilon}_i$ is the irradiation creep rate (hr^{-1})

$\dot{\varepsilon}_s$ is the secondary creep rate (hr^{-1})

ε_p is the primary creep strain

a_i is the irradiation hardening parameter (dimensionless) as a function of fast neutron flunence

E is Young's modulus (MPa)

T is temperature (K)

ϕ is fast neutron flux (n/m^2-sec)

σ_{eff} is the effective stress (MPa)

C = 52 (dimensionless) is a fitting parameter

ε_p^s is saturated primary creep strain

For Stress-Relief Annealed (SRA) material, the parameters used in above equations are: Q = 201 (kJ/mol), a = 650 (dimensionless), n = 2.0 (dimensionless), A = 1.08×10^9 (K/MPa-hr). sec, C_0= 3.557×10-24 ((n/m^2-sec)-C_1(MPa)-C_2/hr), C_1 = 0.85 (dimensionless), and C_2 = 1.0 (dimensionless).The total creep rate is the combination of the primary creep and secondary creep.

$$\varepsilon_c = \varepsilon_p^s[1-\exp(-C\sqrt{\dot{\varepsilon}_s t})] + \dot{\varepsilon}_s t \quad (1\text{-}4)$$

This engineering model describes the creep strain rate as a function of temperature, fast neutron flux/fluence, and stress. Additional details of the numerical implementation and verification of the creep model in the Peregrine code are available elsewhere (Liu et al, 2013).

Figure 1-2 below shows the creep rate (in units of hr^{-1}) calculated using the Limbäck model in the Peregrine code for the SRA zirconium alloys and the range of the in-reactor data that the model was applicable for. Observe that, at higher temperature and/or stress, the contributions of thermal and irradiation creep become comparable.

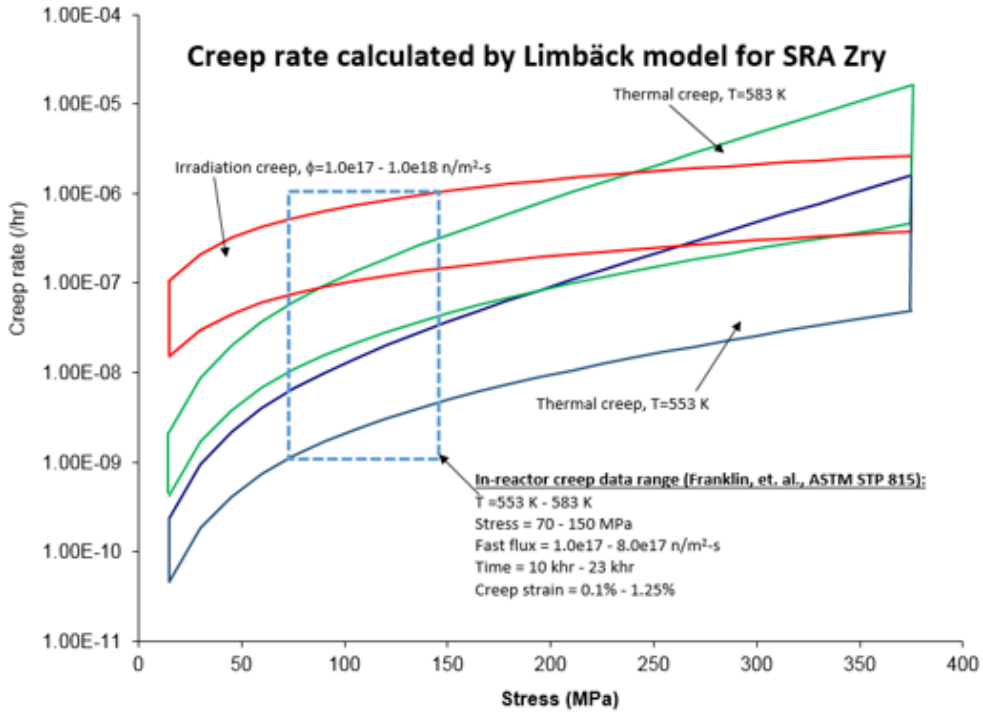

Figure 1-2 Creep rates computed using Limbäck creep model and the range of in-reactor test data

The semi-empirical model described by Equations 1-1 through 1-4 accounts for texture, irradiation, and temperature effects on cladding creep during normal operation and accident conditions where the temperature is less than 500°C. However, without a mechanistic basis for determining the microstructural features that control creep deformation, this model is limited to specific areas of application, namely to the material, stress, and temperature regimes used to develop the model coefficients.

Irradiation growth

Irradiation growth refers to the length increase of zirconium cladding tube caused by irradiation damage in absence of the external stress. In Peregrine, fractional dimension change in the axial direction due to irradiation growth for SRA Zry is computed using Franklin model, which is the same model used in the Falcon fuel performance code.

$$\frac{\Delta L}{L} = A(\phi t)^n \qquad (1\text{-}5)$$

Where ϕt is the fast neutron fluence in n/m^2; A and n are fitting parameters. For SRA material, n = 0.845 and A = 9.09x10^{-25} are used in Peregrine code based on the correlation provided by (Franklin, 1982). For Recrystallized Annealed (RXA) material, A=4.545x10^{-25} is used in Falcon and Peregrine codes.

The basis of the irradiation growth model was summarized in a review paper (Franklin, 1982) which described some of the in-reactor experiments results from three irradiation programs: B&W, CE, and Westinghouse. Among all the 700 measurements on fueled rods from B&W, CE and Westinghouse

programs, not all of them have been characterized, only CE and some of the Westinghouse rods have characterized and were used as the data basis to derive the empirical correlations on irradiation growth. The aforementioned correlation, Eq. (1-5), is based on the measurements on both fuel rods and non-fueled cladding tubes; the measured clad elongation of the fuel rods however may have included some effects due to the pellet-clad interaction, thus the modeled clad elongation may not be caused by irradiation growth alone. As will be shown in Section 2, the mechanisms leading to irradiation growth of the cladding are much more complex than that represented by Equation 1-5, namely the interaction between crystallographic texture characteristics and irradiation damage leading to accelerated growth kinetics that have been observed in certain Zircaloy materials.

Instantaneous plasticity

The empirical equation of clad yield stress is used to model the instantaneous plastic deformation. After clad yielding, the power law, Eq. (1-6), is used to describe the plastic deformation.

$$\sigma = K\varepsilon^{n}\left(\frac{\dot{\varepsilon}}{\dot{\varepsilon}_0}\right)^{m} \tag{1-6}$$

Where,

K = strength coefficient

n = strain hardening exponent

m = strain rate exponent

$\dot{\varepsilon}_0$ = constant, s^{-1}

$\dot{\varepsilon}$ = strain rate, s^{-1}

Clad yield strength is determined using Hooke's Law ($\sigma=E\varepsilon$) to define the stress at yield and equating with Eq. (1-6):

$$\sigma = \left[\frac{K}{E^{n}}\left(\frac{\dot{\varepsilon}}{\dot{\varepsilon}_0}\right)^{m}\right]^{\frac{1}{1-n}} \tag{1-7}$$

The strength coefficient *K*, strain hardening exponent *n*, and strain rate exponent *m* are usually modeled as functions of fast neutron fluence, cold work ratio, and oxygen concentration. A proprietary model used in Falcon code was adapted into Peregrine to compute the clad yield strength. Calculated clad yield strength in comparison to measurement data is shown in Figure 1-3 for several sets of post-irradiation examinations.

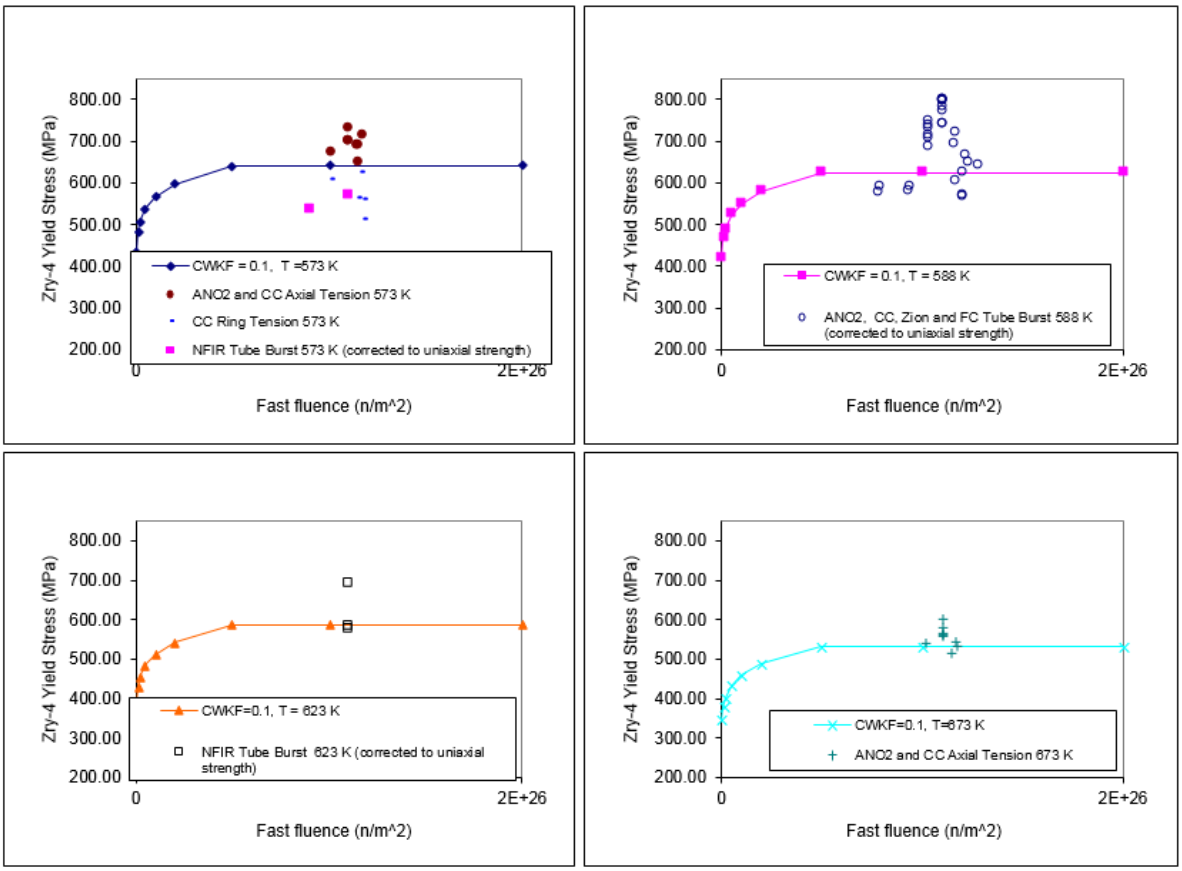

Figure 1-3 Calculated clad yield strength in comparison to measurement

The engineering models summarized in simple equations are easy to use and have played important roles in the fuel performance codes for modeling fuel rod mechanical response. However, one must be aware of the limitations of such models and their applications. Empirical fitting parameters used in the engineering models to account for different mechanisms often lack a physical basis, and the model may only be applicable to the test conditions used for the fitting procedure, and not over ranges where the models have not been verified. The statistical significance of the measurement data is an important factor that determines the predictability of the model. However the complexity of the irradiation environment and variations in the test specimen and test conditions could lead to inconsistencies among different models used in different fuel codes.

To improve the model predictability, relying solely on advanced computational methodologies is not sufficient, and more physical behavioral models are desired for interfacing with the traditional fuel performance codes. Improved compiling and interpretation of measurement data could help but perhaps it would only be limited to the information that can be provided in experiments, and some information required for model improvement might be missing.

1.3 Peregrine and Microscale Fuel Behavior Modeling

The Peregrine fuel performance code (Montgomery et al, 2012) is an engineering scale finite element method (FEM) code that is built upon the MOOSE/ELK/FOX structure/architecture, which is also common to BISON (Gaston, 2009 and Williamson, 2012). Peregrine uses both 2-D and 3-D geometric fuel rod representations and a material property and fuel behavior model library for the

UO_2 and Zircaloy system to accurately calculate the thermal, mechanical, and chemical processes active throughout a single LWR fuel rod during operation in a reactor, for both steady state and off-normal conditions. The Peregrine framework consists of a numerical representation of the heat conduction and the equilibrium mechanics equations, which are coupled via the temperature and displacement variables using the MOOSE/ELK/FOX architecture.

Figure 1-4 provides an overview of the major components in Peregrine and some of the functionality included in each component. There are six major components within Peregrine that together provide the functionality to perform fuel performance calculations. The computational framework in MOOSE provides four of the components: Problem Setup, Physics Solution, Global Parameters Integration, and Results Output as native elements that can serve as building blocks for Peregrine. This has simplified the development time for Peregrine and allowed the rapid advancement of multi-dimensional finite element representation of a fuel rod and detailed analyses using existing material property models from Falcon.

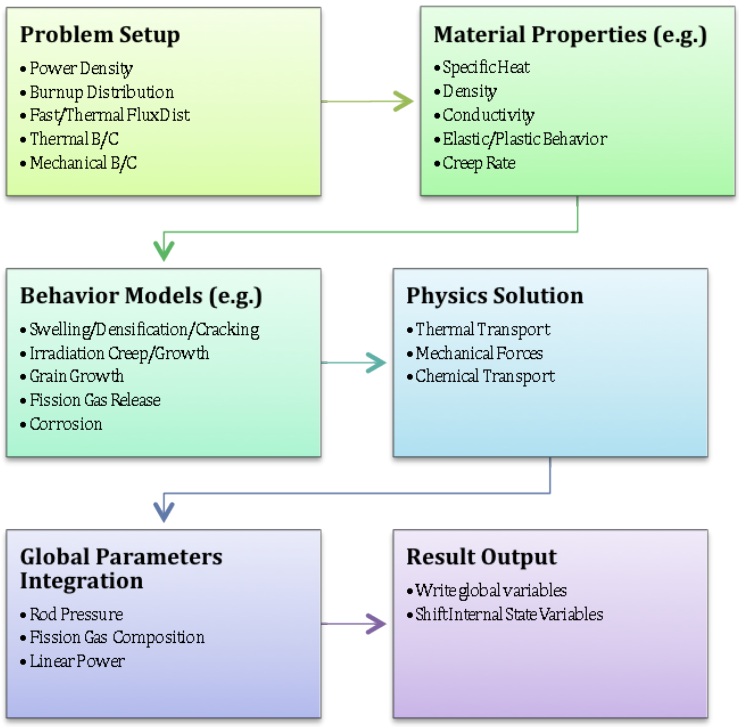

Figure 1-4 Schematic of Peregrine code structure

Peregrine contains a material and constitutive properties library that allows for thermal, mechanical, and chemical property models and irradiation effects models, such as fission product-induced swelling, irradiation creep, fission gas release, and pellet cracking. This library is based on open literature empirical models from the MATPRO package developed by NRC (Hagrman et al., 1981) and select models from the EPRI fuel performance code, Falcon (Montgomery et al, 2004 and Rashid et al., 2004). The empirical/semi-empirical material and behavior models currently incorporated into Peregrine provide the ability to replicate the existing fuel modeling capabilities in established codes such as FRAPCON (Geelhood et al. 2011) and Falcon (Montgomery et al., 2004 and Rashid et al., 2004). This provides an excellent starting point for identifying areas for improvement in key material property or behavior models using advanced modeling and simulation capabilities.

The fuel behavior model development activities in CASL consists of three different length and time scales: (1) the engineering scale 2D/3D finite element fuel behavior code to capture integral fuel rod behavior, (2) microscopic length scale model development to account for the texture, microstructure, alloy contents, and lattice damage network on cladding creep and growth, clad hydride formation, and waterside corrosion, and (3) atomistic length scale modeling to provide improved understanding of diffusion coefficients and chemical reaction kinetics associated with fission gas release, fission product attack of the cladding, and corrosion. A key focus of the CASL material modeling effort is to develop more in-depth physics-based models for irradiation creep and growth, thermal creep, outer cladding surface corrosion, inner surface cladding corrosion, fission product release and transport, and ceramic material fracture behavior.

Several activities, either on-going or planned within CASL, have started to address the needed capabilities for advanced modeling of fuel behavior during normal, operational transients, and accident events. One of these efforts is the expansion of a microstructure-based deformation model using the Visco-Plastic Self-Consistent (VPSC) approach to calculate thermal and irradiation creep, irradiation growth, and plastic deformation of the cladding. A schematic of the microstructure-aware, atomistcally-informed approach to cladding deformation modeling is shown in Figure 1-4. The approach consists of deploying an enhanced version of VPSC where the constitutive framework is based on dislocation density behavior (from the seminal work of Beyerlein and Tomé (2008)). VPSC is interfaced with Peregrine to obtain the environmental conditions, macroscopic stress field, temperature, and neutron fluence. Finally, the goal is for VPSC to obtain information on reaction rate kinetics from atomistic calculations. The approach outlined in Figure 1-4 represents a quantum leap forward in modeling the effects of the irradiation environment on cladding deformations.

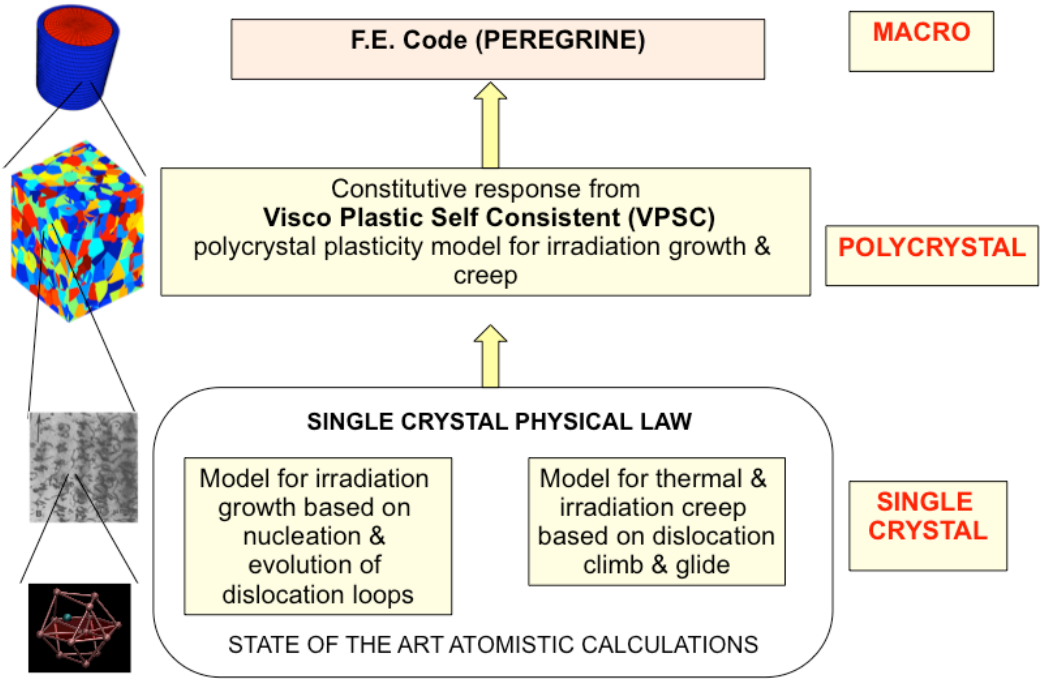

Figure 1-4. Microstructurally-aware, atomistcally-informed cladding deformation model approach

The single crystal formulation in VPSC accounts for the vacancy and interstitial loops in the cladding created by irradiation. It also accounts for the climbing of those loops through defect capture, and for their interaction with mobile dislocations on active slip systems at the microscale. The polycrystal model in VPSC then aggregates the effect of activating these slip or twinning systems by dislocation behavior within single grains, and combining this with crystallographic texture information, calculates the dimensional changes in the material. The constitutive equations in VPSC that account for stress or irradiation-induced deformation are functions of activation energies for dislocation motion or reaction constants (sink or emission strengths) that define the interaction kinetics between dislocations and other microstructure features such as interstitials, vacancies, grain boundaries, and other dislocations. While established values are available for these interaction constants/parameters, this framework provides a method to utilize information obtained from atomistic calculations that can expand or improve the formulations in VPSC.

For example, Subramanian et al. (2012, 2013), recently performed a series of atomistic simulations using both molecular dynamics (MD) and kinetic Monte Carlo (kMC) methods to study the absorption rate of point defects (self interstitial atoms and vacancies) by various sinks, such as edge dislocations within zirconium crystals. Motivated by the dislocation dynamics rate equations used by VPSC to compute creep and growth processes, Subramanian et al. focused on providing improved understanding of point defect absorption rates, accounting for variations in strain fields in the material. While still under development, this method will allow more accurate computation of parameters, such as sink strength and sink efficiency of dislocation networks that are used in traditional radiation damage models. Accurate computations of point defect absorption rates are critical for calculating mesoscale phenomena, such as dislocation climb and loop growth, which determine microstructural evolution under irradiation. In the area of irradiation growth, Golubov et al. (2011,1013), have developed a reaction-diffusion model for single crystal irradiation growth of zirconium material that considers the formation of defects by displacement cascades and the accompanying diffusion of defect clusters to dislocations. This model has been interfaced with VPSC for comparison to polycrystalline data on irradiation growth.

1.4 Conclusion

Traditional models used for the simulation of fuel elements are mostly based on empirical fitting of experimental data and the introduction of empirical parameters that have little or no connection with the actual physical mechanisms responsible for the mechanical behavior. As a consequence, their application is limited to the range of cladding tube microstructure, and temperature, dose and stress state conditions utilized for performing such fitting. Extrapolating these models to other conditions, such as abnormal operation or accident conditions, is not justified and the predicted results may be erroneous. As a consequence, there is a need to improve our predictive cladding capabilities, and base those on models based on physical material mechanisms and microstructure evolution during irradiation.

2. CONSTITUTIVE MODELS IN VPSC

2.1 Basic paradigm

In this Section we describe the models developed to describe the constitutive response of cladding subjected to irradiation: we identify 4 different regimes, depending on temperature and stress. The regimes of relevance for plasticity of Zirconium are sketched in Figure 2-1(a) (Sargent and Ashby, 1982) as a function of the temperature and stress interval involved. We adapt this representation for our purposes, where we need to account for irradiation effects. The mechanisms involved are: 1) irradiation growth and irradiation creep, which dominate at reactor operating temperatures ($T > 0.3T_M$) and at lower stresses ($0.3\ \sigma_F < \sigma < 0.7\ \sigma_F$), are mediated by the climb of dislocations (growth) and by climb-controlled-glide of dislocations (creep), and driven by a large concentration of irradiation-produced vacancies and interstitials; 2) thermal creep ($T > 0.5T_M$ and $\sigma > 0.7\ \sigma_F$), mediated by climb and glide of dislocations due to absorption/emission of vacancies, which are abundant at high temperature; 3) instantaneous plasticity ($\sigma > 0.9\ \sigma_F$): mediated by creation and glide of dislocations with stress-induced activation over barriers. A rough deformation map would look like the one in Figure 2-1(b), with the understanding that the domains represent conditions where a particular mechanism prevails, but does not exclude that other mechanisms are simultaneously active.

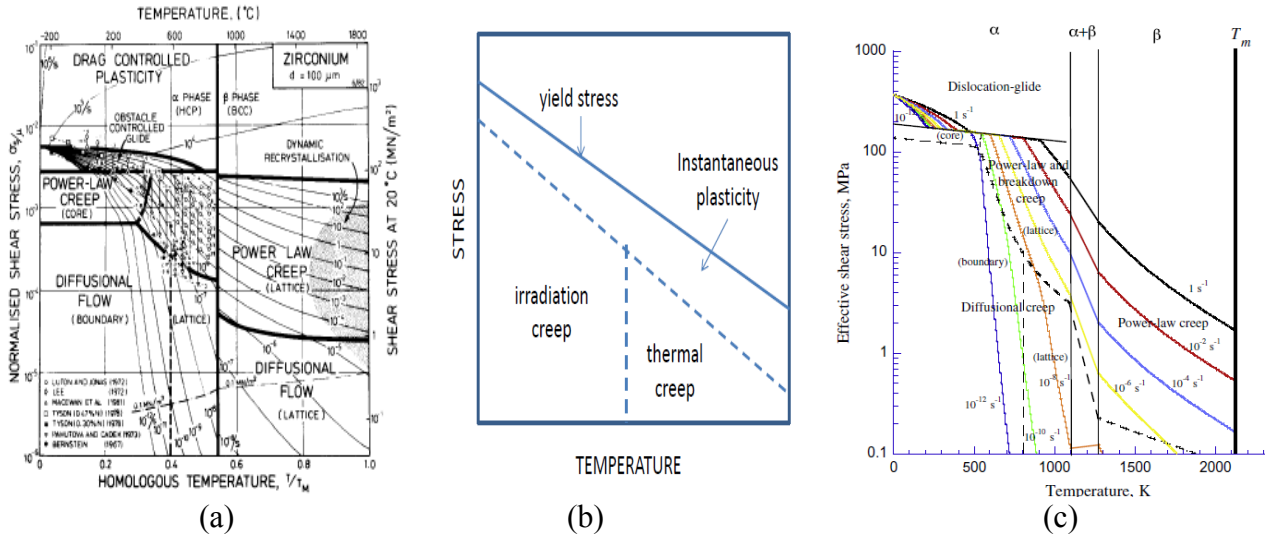

Figure 2-1 (a) Ashby map for Zr; (b) schematic map of mechanism for irradiated Zr alloys; (c) thermal creep for unirradiated Zircaloy-4 (Wang et al, 2013)

Because all the mechanisms are mediated by dislocations, and because dislocations have specific orientations in the Zr crystals, it makes sense to adopt a Crystal Plasticity (CP) Model of the material which accounts not only for the directionality of dislocations in the crystal lattice, but also for the distribution of crystal orientations in the cladding tube (texture). In addition to explicitly accounting for anisotropy, such a CP model has the advantage of being based on the actual physical mechanisms of dislocation glide and climb (plasticity), dislocation-dislocation interaction (hardening), dislocation-vacancy interaction, and dislocation interstitial interaction (growth).

2.1.1 Visco Plastic Self Consistent Model

The fully anisotropic visco-plastic self-consistent (VPSC) polycrystal plasticity model originally developed by Lebensohn and Tomé (1993) has seen continuous improvements since then. An updated comprehensive description of the method can be found in Lebensohn et al (2004). In brief, the metallic aggregate (polycrystal) is represented by weighted orientations (crystals): the orientations represent grains and the weights represent volume fractions. The latter are chosen to reproduce the texture of the aggregate. Each grain is treated as an ellipsoidal visco-plastic inclusion embedded in an effective visco-plastic medium. Both, inclusion and medium have fully anisotropic properties. The effective medium represents the 'average' environment 'seen' by each grain (Fig. 2-2).

When boundary conditions of stress or strain rate are applied to the effective medium, an interaction between medium and grain (embedded inclusion) takes place, and local stresses are induced in the inclusion and its vicinity, which drive the deformation of the inclusion. The stresses, which follow from solving the stress equilibrium equations, deviate from the average stress in the medium, depending on the relative properties of medium and inclusion. The 'self consistency' of the approach relies on enforcing the condition that the average stress and strain rate over all the grains has to be equal to the boundary values imposed on the medium.

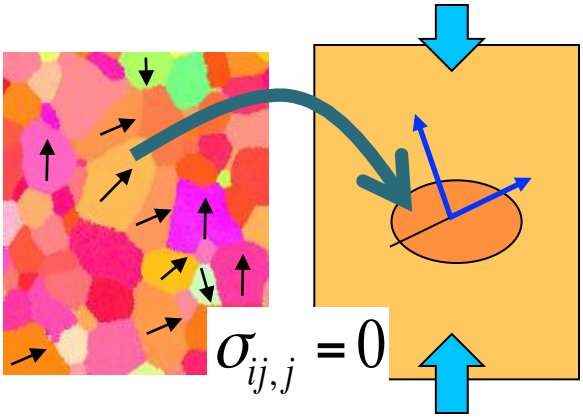

Figure 2-2 Schematic showing the representation of a grain and its surrounding as an ellipsoidal inclusion embedded in an effective medium. The interaction with the medium determines the stress and strain rate of the inclusion

Dislocations propagate in compact atomic planes producing plastic shear and no volumetric dilatation. Let us denote ns the normal to the slip plane, and b^s the direction of shear (Burgers vector). If σ_{ij} is the stress tensor acting on the crystal (grain) then the resolved shear stress on the shear plane and along the shear direction is given by

$$\tau^s_{res} = b^s_i n^s_j \sigma_{ij} = m^s_{ij} \sigma_{ij} \qquad (2\text{-}1)^{\#}$$

Where the Schmid tensor is defined as: $m^s_{ij} = \frac{1}{2}(b^s_i n^s_j + b^s_j n^s_i)$.

[#] Unless stated otherwise, throughout this text we use the implicit summation convention: repeated indices in equations denote summation over the range of such indices.

The dislocation climb and glide systems that we will consider in HCP Zr crystals are depicted in Figure 2-3. The glissile dislocations are: {1010}<1120> prism slip (3 systems), {0001}<1120> basal slip (3 systems), {1011}<1123> pyramidal slip (12 systems). The sessile dislocation loops are one basal (0002) <0002> and three prism {1120}<1120>. The experimental information indicates that the former usually has a vacancy stacking fault configuration, and the latter an interstitial stacking fault configuration.

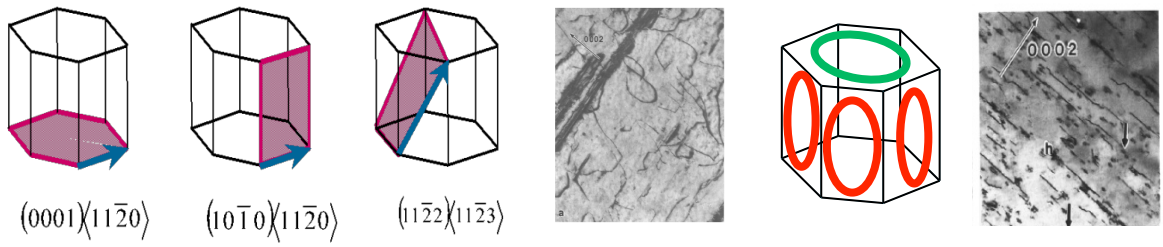

Figure 2-3: Basal, Prism and Pyramidal dislocations introduced by tube manufacturing process; microstructure of unirradiated Zrly-2; prism and basal dislocations loops introduced by irradiation; microstructure of irradiated Zrly-2

The shear rate $\dot{\gamma}^s$ in system *s* has associated a strain rate tensor in given reference axes

$$\dot{\varepsilon}_{ij}^c = m_{ij}^s \dot{\gamma}^s \tag{2-2}$$

And the visco-plastic constitutive law states that shear rates are represented by a power law of the ratio between resolved shear and a threshold stress

$$\dot{\gamma}^s = \dot{\gamma}_o \left(\frac{m_{kl}^s \sigma_{kl}}{\tau_{thres}^s} \right)^n \tag{2-3}$$

where $\dot{\gamma}_o$ is a normalization factor and *n* is the rate-sensitivity exponent. When several systems are active in a grain, the strain rate is given by the sum of their shear rates

$$\dot{\varepsilon}_{ij} = \sum_s m_{ij}^s \dot{\gamma}^s = \dot{\gamma}_o \sum_s m_{ij}^s \left(\frac{m_{kl}^s \sigma_{kl}}{\tau_{thres}^s} \right)^n \tag{2-4}$$

Linearizing Eq. (2-4) inside the domain of a grain gives:

$$\dot{\varepsilon}_{ij}^c = M_{ijkl}^c(\sigma) \sigma_{kl}^c + \varepsilon_{ij}^{o(c)} \tag{2-5}$$

where M_{ijkl}^c and $\varepsilon_{ij}^{o(c)}$ are the viscoplastic compliance and the back-extrapolated term of grain (c), respectively. The linearization (2-5) of the constitutive response is required to solve the equilibrium conditions between inclusion and medium, and is actually a tangent approximation to the non-linear law (2-4). The constitutive law giving the response of the effective medium (polycrystal) is given by a linear relation analogous to (2-5):

$$\bar{\dot{\varepsilon}}_{ij} = \bar{M}_{ijkl} \bar{\sigma}_{kl} + \bar{\dot{\varepsilon}}_{ij}^o \tag{2-6}$$

where $\bar{\dot{\varepsilon}}_{ij}$ and $\bar{\sigma}_{kl}$ are overall (macroscopic) magnitudes and $\bar{M}_{ijkl}$ and $\bar{\dot{\varepsilon}}_{ij}^o$ are the macroscopic viscoplastic compliance and back extrapolated rate, respectively. The latter moduli are unknown *a priori* and need to be adjusted self-consistently.

2.1.2 Texture and discrete texture representation

Metallic materials are formed by crystallographic domains called grains (shown in the EBSD microscopy of Fig 2-2 with a superimposed c-axis direction). The distribution of orientations of the crystal structures associated with each grain (such as the hexagonal cell shown in Fig. 2-3) is called *texture*. Preferential orientations are called *texture components,* and are characteristic of the fabrication process (e.g. rolling, extrusion, torsion). The importance of texture is that it determines the anisotropy of the mechanical response of materials (e.g. the directional strength of a particular

texture component may dominate the mechanical response of the polycrystal). As a consequence, accounting for texture in modeling allows us to predict anisotropic behavior.

In the case of hexagonal polycrystals, it is common to represent the orientation of the c-axis (basal texture) of the grains in what is called a 'pole figure'. The procedure for producing a pole figure is sketched in Fig. 2-4. In brief: each grain is thought as 'positioned' in the center of a sphere; the normal to the plane being represented (c-axis in our case) is extended until it intersects the sphere; a line joining a pole in the sphere and the intersection point is made to intersect a 2D plane, called the 'projection plane'. When many such points (each representing one grain) are projected onto the 2D plane they define a density of points per unit area (intensity), which describes concentration of grains with similar c-axis orientation. It is usual to represent such density using iso-intensity level lines, such as the ones on the right of Fig. 2-4, which corresponds to an extruded cladding tube. In this particular case the extrusion process tends to concentrate the c-axes on the Hoop-Radial plane, with two maxima at about +30° and -30° from the radial sample axis.

The texture is measured using X-ray diffraction or Electron Back Scattering Diffraction (EBSD) in a scanning microscope (Kocks et al, 1999) and for modeling purposes it is converted into a discrete collection of crystal orientations, typically composed of 1000 to 3000 grains. Polycrystal Plasticity codes use this collection as the material representation, and keep track of the stress, strain, crystal orientation, activity and activation stress in each slip system in each grain, dislocation density on each slip system, etc. The response and properties of such aggregate is given by averaging the response and the properties of the individual constituent grains.

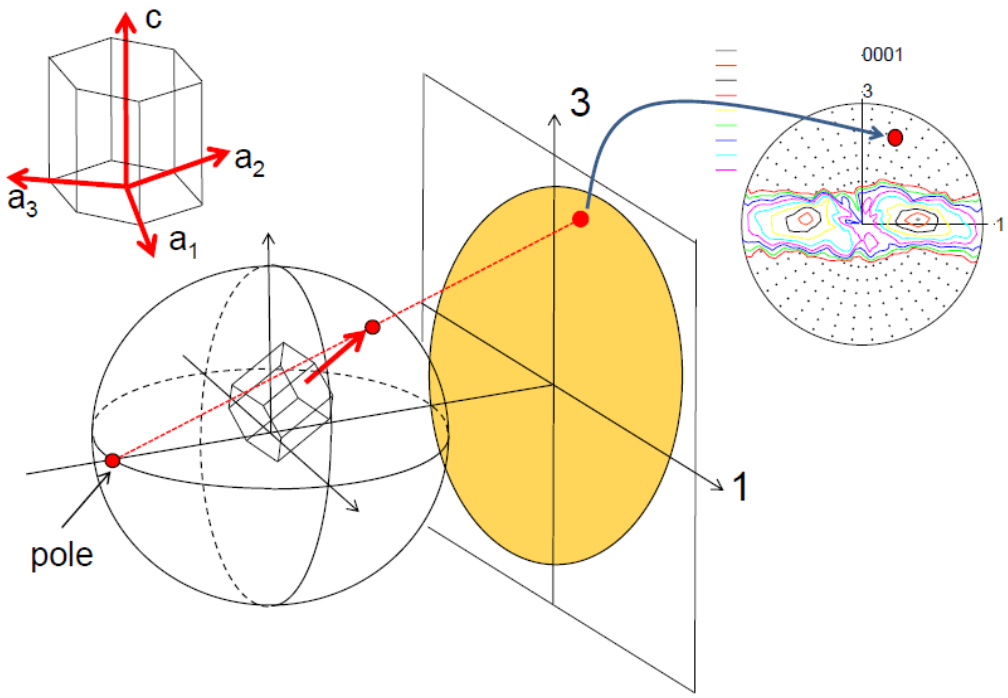

Figure 2-4: Crystal axes associated with the hexagonal crystal cell; schematic of polar projection of the c-axis onto the 2D pole figure; actual pole figure of cladding represented by means of intensity lines

2.2 Irradiation Growth & Irradiation Creep

Neutron irradiation produces vacancies, interstitials and interstitial clusters in irradiated Zr alloys, with concentrations far greater than their thermal equilibrium concentrations. These defects eventually get absorbed by sinks, such as forest dislocations and dislocation loops, and produce dimensional changes in the material. When dislocations preferentially absorb vacancies or interstitials, they climb. Dislocation climb may be followed by glide (climb assisted glide) in the presence of a resolved shear stress. Both mechanisms induce dimensional changes, and are called irradiation growth and irradiation creep, respectively, and are driven by a high concentration of irradiation-produced defects.

Irradiation growth is the irradiation-induced dimensional changes that take place in the absence of applied stresses, and is caused by the trapping of vacancies and interstitials by sinks present in the crystal (i.e.: dislocations, grain boundaries). Each sink makes a directional contribution to the macroscopic strain, such that the final deformation is anisotropic and volume conserving. In Zr alloys point defects tend to aggregate into either mobile (glissile) dislocations or immobile (sessile) dislocation loops, making them climb and grow in size, and thereby changing the crystal dimension perpendicular to the plane of the loop. Irradiation creep is low-rate plastic deformation that occurs at stresses and temperatures relevant at reactor operating conditions ($T > 0.3T_M$ and $0.5\ \sigma_F > \sigma > 0.3\ \sigma_F$),

The two phenomena of irradiation creep and irradiation growth become coupled in polycrystalline materials. This is because the growth of a grain induces reaction stresses that result from the grain interaction with its neighbors (which are also growing but generally not at the same directional rate). These stresses, in turn, induce irradiation creep in the grains, even if at the macroscopic level the material is stress-free. Under some non-standard operating conditions, internal stresses may be high enough so that thermal creep becomes important and helps relax the internal stress. A distinguishing feature of our polycrystal approach is that it accounts explicitly for these internal stresses and the creep-growth coupling, a feature that is absent in empirical continuum models used in reactor simulations: they describe each of these regimes independently and as a function of only the macroscopic boundary conditions.

In a previous CASL report [Subramanian and Tomé, 2012] we described the incorporation of an irradiation growth model for single crystal Zr developed by [Golubov et al, 2011, 2013; Barashev et al, 2012] into the VPSC framework. The most relevant feature of Golubov's model is to postulate that the interstitial clusters created during neutron irradiation are 1D diffusers on the basal plane, while vacancies and interstitials are 3D diffusers. By requiring this behavior to be consistent with irradiation growth experiments of a single crystal performed by Rogerson and Zee [1987], Golubov et al deduce empirically a rate of nucleation of dislocation loops with dose. Essentially, interstitial loops nucleate early on prism planes, and vacancy loops nucleate later in basal planes. The actual nucleation rate vs dose and evolution of loops radius vs dose is illustrated in Figure 2-5.

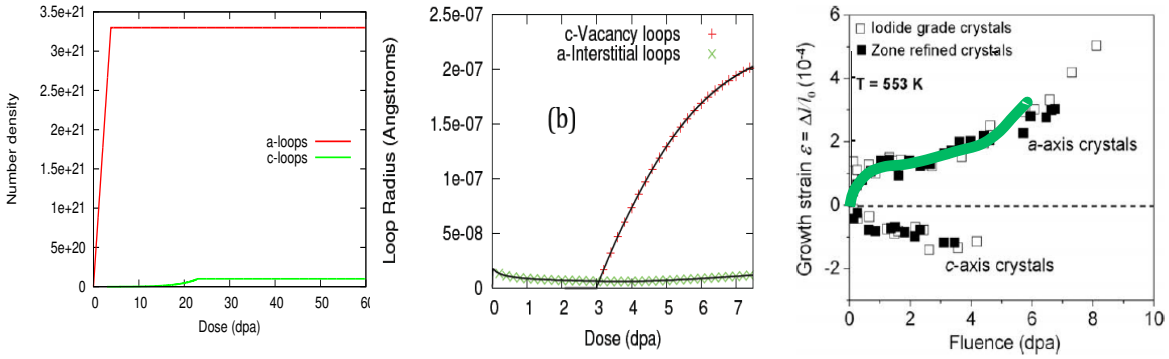

Figure 2-5: (a) Rate of loop nucleation proposed by Golubov et al [2011]; (b) predicted evolution of average loop radious vs dose (red: interstitial prism loops; green: vacancy basal loops); (c) experimental growth measured by Rogerson and Zee [1987] in single crystal and evolution predicted by the model.

In this paper, we describe the generalization of Golubov et al's Reaction-Diffusion model to incorporate the full crystallography required by VPSC. We also include in the model a fully crystallographic mechanism of Climb-Controlled Glide (CCG), added recently by Golubov et al [2013] to their growth model to account for creep effects. We first describe the Fully Crystallographic Irradiation Growth model, and then discuss its implementation into the VPSC framework, and the implementation of a Climb-Controlled-Glide model.

Assume N different dislocation lines s with density ρ_s oriented along $\hat{l}_s$ and moving with velocity $\bar{v}_s$ inside a grain. The total velocity gradient tensor that results from the summation over all the dislocations is given by [Woo, 1985]

$$\dot{u}_{m,n} = \frac{\partial \dot{u}_m}{\partial x_n} = \sum_{s=1}^{N} \rho_s \left(\hat{l}_s \times \bar{v}_s \right) \otimes \bar{b}_s \tag{2-7}$$

Where $\times$ and $\otimes$ represent the vector product and the dyadic product, respectively. For straight edge dislocations the direction of climb velocity is normal to the glide plane and $\left(\hat{l}_s \times \bar{v}_s \right) \otimes \bar{b}_s = v_s b_m b_n$. For loops the direction of climb is normal to Burgers vector and contained in the loop plane, and $\left(\hat{l}_s \times \bar{v}_s \right) \otimes \bar{b}_s = v_s n_m n_n$. Here $v^s = \dot{N}_{i \to s} - \dot{N}_{v \to s}$ is the number of interstitials minus the number of vacancies absorbed by the dislocation s per unit time and unit length. Golubov et al [2013] model provides such rate for forest dislocations and loops as a function of the irradiation dose, and we use their result in our implementation. Finally

$$\dot{u}_{m,n} = \frac{\partial \dot{u}_m}{\partial x_n} = \sum_{s=1}^{N} (\dot{N}_{i \to s} - \dot{N}_{v \to s}) \rho^s \left(\hat{l}_s \times \hat{n}_s \right) \otimes b^s \tag{2-8}$$

The strain rate is the symmetric component of the velocity gradients associated with climb of the edge component of the mobile dislocation systems and climb of the sessile dislocation loops:

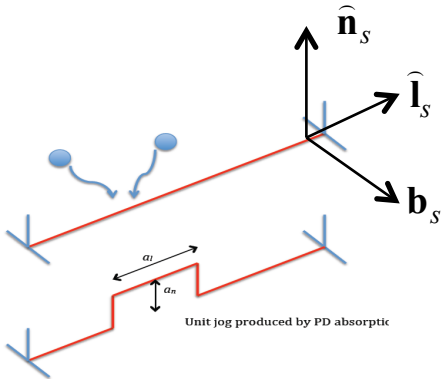

$$\dot{\varepsilon}_{mn}^{growth} = \frac{1}{2}(\dot{u}_{m,n} + \dot{u}_{n,m}) = \frac{1}{2}\sum_{s=1}^{N_s}(\dot{N}_{i\to s} - \dot{N}_{v\to s})\rho^s(b_m^s b_n^s + b_n^s b_m^s) + \frac{1}{2}\sum_{l=1}^{N_l}(\dot{N}_{i\to l} - \dot{N}_{v\to l})\rho^l(n_m^l n_n^l + n_n^l n_m^l) \tag{2-9}$$

Figure 2-6: Schematic of edge dislocation climb and dislocation-associated vectors

Next, for incorporating irradiation creep into the model, we adopt the relatively simple climb-controlled-glide model of Gittus [Gittus, 1977; Heald and Harbottle, 1972]. In this model the shear rate of a dislocation segment is proportional to the resolved shear acting on the segment and inversely proportional to the time it takes to climb over obstacles. The latter is taken here as the average radius of loops r_{mean} divided by the climb velocity v^s. The shear contributed by a dislocation system is also proportional to the availability of segments, namely, to the density.

$$\dot{\gamma}^s = \rho^s \frac{m_{kl}^s \sigma_{kl}}{\mu} \frac{v^s}{r_{mean}} \tag{2-10}$$

And the total creep that results from all dislocations that climb-glide is:

$$\dot{\varepsilon}_{ij}^{creep} = \sum_{s=1}^{N} m_{ij}^s \dot{\gamma}^s = \sum_{s=1}^{N} m_{ij}^s \rho^s \frac{m_{kl}^s \sigma_{kl}}{\mu} \frac{v^s}{r_{mean}} \tag{2-11}$$

Where σ_{kl} is the stress in the grain; m_{ij}^s is the Schmid tensor that projects the stress onto the slip plane of system s; ρ_s is the glissile dislocation density for this system; v_s is the climb velocity of the *glissile* dislocations; μ is the shear modulus.

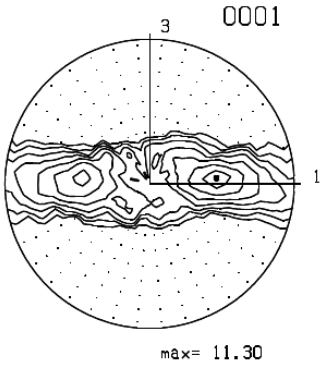

We identify the sum of growth and creep rates given by Eqs (2-9) and (2-11) with the general form of the strain rate that enters in the VPSC formulation (Eq 2-5),

$$\dot{\varepsilon}_{ij} = M_{ijkl}(\sigma)\sigma_{kl} + \varepsilon_{ij}^o = \varepsilon_{ij}^{creep} + \varepsilon_{ij}^{growth} \tag{2-12}$$

and apply the VPSC model to predict the dimensional changes of a cladding tube subjected to irradiation and stress. We utilize a typical cladding tube texture shown in Fig 2-7, and represented here using 1992 grains with assigned volume fractions consistent such as to reproduce an experimentally measured texture.

Figure 2-7: basal pole figure corresponding to a cladding texture represented by 3000 grains (1:hoop, 2:radial; 3:axial direction)

In what follows we simulate the dimensional changes of cladding under irradiation but in the absence of applied stress (macroscopic 'growth'). As mentioned above, grain growth will trigger

internal stresses coming from the interaction with the grain surroundings, and the latter will activate irradiation creep inside the grain. Macroscopically, those internal stresses average to zero but the dimensional changes produced by creep do not. In what follows, we also explore the role that the initial dislocation density (introduced by the tube fabrication process) has on the macroscopic growth predicted.

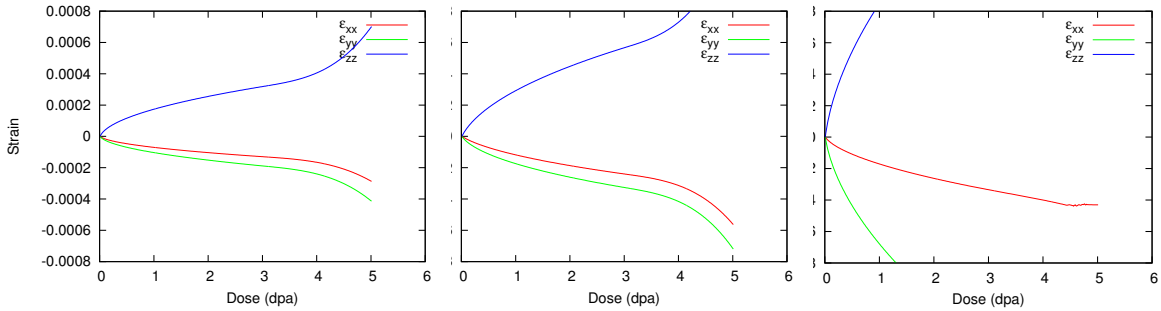

Figure 2-8: Dimensional changes of cladding vs dose in the absence of applied stress. (a) Reference case $\rho_{basal} = \rho_{prism} = \rho_{pyram} = 10^{11} m^{-2}$ (b) Increasing Prismatic dislocation density by a factor 10 (c) Increasing Pyramidal dislocation density by a factor 10 (x=hoop, y=radial, z=axial)

Several features of these predictions are worth noting: 1) the fact that the texture of the tube has a majority of prism planes along the axial direction, and that interstitial loops tend to nucleate and grow in prism planes, gives positive growth along the axis; 2) the delayed nucleation of vacancy loops (Fig 2-5a) leads, when they start nucleating, to shrinkage of the grain c-axis and accelerated expansion (due to volume conservation) of the basal directions. This 'accelerated growth' is clear in Fig 2-8a past a 4 dpa dose; 3) when the density of initial glissile dislocations is large, the growth rate increases. In addition, more forest dislocations tend to trap defects more efficiently, and so delay the trapping by loops, even if they have nucleated. As a consequence, 'accelerated growth' is delayed. A good example is the case of Fig 2-8c, with a large initial density of pyramidal dislocations, where 'accelerated growth' has been suppressed for the dose interval considered.

Next we investigate the effect of stress superimposed with irradiation, in which case the mechanism of climb-controlled-glide is activated. In this case we impose initial dislocation densities on individual slip systems $\rho_{basal} = \rho_{prism} = \rho_{pyram} = 10^{11} m^{-2}$, consistent with annealed material. Observe that an axial stress of 100MPa increases the rate of axial deformation, as is to be expected (Fig 2-9b). When a hoop stress of 200 MPa is added to the 100 MPa along AD the resulting state corresponds to internal pressurization of the cladding tube. Because in creep it is the deviatoric stress that counts, now the deviatoric component along the AD is negative and, as a consequence, the response changes considerably: the positive creep strain induced along the HD now compensates the negative growth strain, and the condition negative creep strain along the AD reduces the positive growth strain (Fig 2-9c)

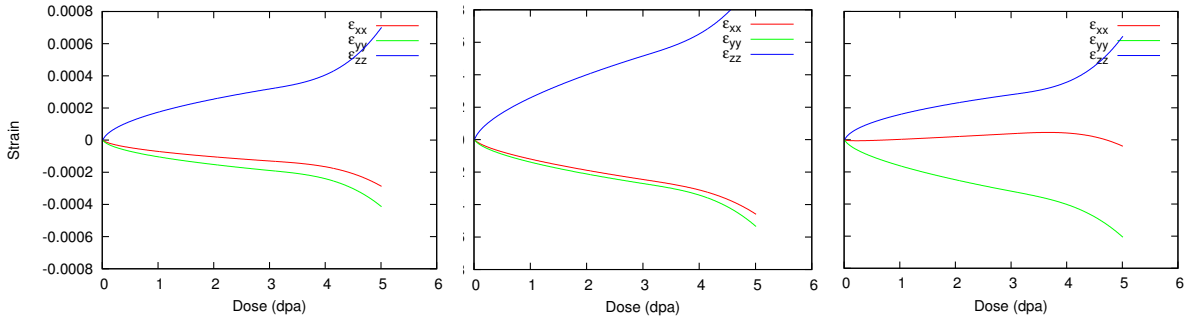

Figure 2-9: Response of the full tube texture (3000 grains) and initial densities $\rho_{basal} = \rho_{prism} = \rho_{pyram} = 10^{11} m^{-2}$. (a) No load; (b) 100 MPa along Axial Direction (z); (c) 200 MPa along Hoop (X-direction) and 100 MPa along Axial (Z-direction)

Next we select two grains from the 3000 grain texture to illustrate the evolution of internal stress inside them as a function of dose (Fig 2-10). One grain has the c-axis oriented along the AD, far away from the orientation of most of the grains in the tube. As a consequence, when inserted in the effective medium the directional properties of this grain are going to be very different from the ones of the medium and the interaction is expected to be strong. The other grain has the c-axis oriented along the HD and, although it does not coincide with any of the main texture components of Fig 2-7, it is closer to those. In Fig 2-10 we report the diagonal stress components expressed in the axes of the coordinate system attached to the grain and, therefore, σ_{zz} is the normal stress along the c-direction of the grain.

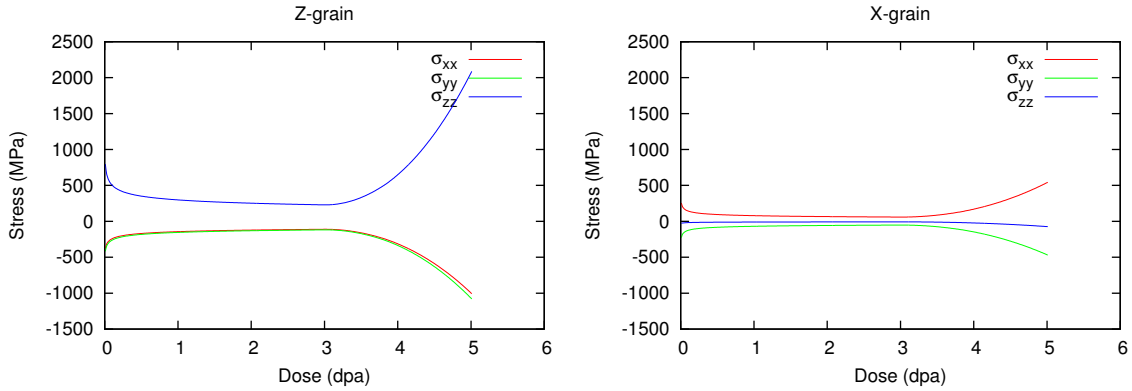

Figure 2-10: Evolution of main stress components with dose in individual grains of the 3000-grain polycrystal. (a) The grain designated as Z has the c-axis oriented along the AD; (b) the grain designated as X has the c-axis oriented along the HD. The stresses are expressed in sample axes (HD, RD, AD).

This result illustrates an important capability of the polycrystal model, namely, the coupling of growth and creep inside the grains. The initial trend for the Z-grain is to expand by growth perpendicular to the c-axis (//AD), but the tendency of the effective medium is to contract in that direction and, as a consequence, it induces strong back stresses of order 500 MPa inside grain Z. Those stresses tend to relax (by irradiation creep) as dose accumulates but, when 'breakaway growth' takes place the initial situation returns and stresses increase very rapidly. While for the doses considered here there is still no sign of relaxation, eventually those internal stresses will stabilize when growth and irradiation creep compensate each other. While in this case we did not account for the contribution of thermal creep (to be described in next section), it is likely that even at

the relatively low reactor operating temperature thermal creep will be activated at such high stress values, which will relax the growing stresses. Inside the second grain the internal stresses are much lower, but they also tend to increase with the appearance of breakaway growth. Note that for these simulations the cladding tube was not externally loaded, and so the net stress is zero.

2.3 Thermal Creep

Thermal creep takes place by glide of dislocations cutting the dislocation or obstacle forest via stress and temperature activated mechanisms of diffusion. As such, it is relevant at relatively high temperatures ($T > 0.5T_M$) or applied stresses approaching the flow stress ($\sigma > 0.75\ \sigma_F$). While thermal creep is not a major player under normal reactor operating conditions, it becomes important under abnormal or accident conditions, where localized temperature and stress rises can take place. The power law expressed by Eq. (2-4) is appropriate for describing the contribution of several slip systems to the total creep in a grain

$$\dot{\varepsilon}_{ij} = \sum_s m_{ij}^s \dot{\gamma}^s = \dot{\gamma}_o(T) \sum_s m_{ij}^s \left(\frac{m_{kl}^s \sigma_{kl}}{\tau_{thres}^s} \right)^n \tag{2-13}$$

As in the case of irradiation creep, here we assume that glide takes place in prism, basal and pyramidal planes. The parameters that enter in Eq. (2-13) are related to physical properties of Zr alloys, and are described in what follows. The reference shear $\dot{\gamma}_o$ depends on temperature and the activation energy for the diffusion controlled mechanism. Here we use a dependence derived by Christodoulou et al (2002) from fitting a comprehensive database of tensile and shear creep experiments done on a Zr-2.5%Nb alloy tubes, at different temperatures and imposing different stresses along different directions. Their expression assumes that $\dot{\gamma}_o$ is the same for all systems, which is a simplification, and assign the specific dependence of creep for each system to the threshold value τ_{thres}^s . Christodoulou et al (2002) report:

$$\dot{\gamma}_o(T) = \dot{\gamma}_o(T = 523) \exp\left[-Q(T) \left(1/T - 1/523 \right) \right] \tag{2-14}$$

Where $\dot{\gamma}_o(T = 523) = 4.157 \times 10^{-3} h^{-1}$

and $Q(T) = \left(5000 + \frac{5600}{1 + e^{-(T-470)/15}} \right)$

Observe that the pre-exponential factor in Eq. (2-14) varies with temperature, suggesting that the character of the activation mechanism may be changing with temperature. Since the temperature interval covered by the experiments is 373K <T <596K, using this expression for simulating abnormal conditions (such as tube ballooning, discussed in Section 4) may not be appropriate. The experiments of Christodoulou et al suggest an interval $3.8<n<4.2$ for the rate sensitivity parameter, similar to the range $3.4<n<4.6$ reported from deduced from the data compilation for Zrly-4 by Wang et al. (2013). In our model we adopt $n=4$. The threshold stresses that appear in Eq (2-13) that fit the data shown in Fig 2-11c are τ_{thres}^s=0.100, 0.111, 0.300 GPa for prism, basal and pyramidal glide, respectively. We reproduce below some of the data reported by Christodoulou et al (2002) using the parameters quoted above.

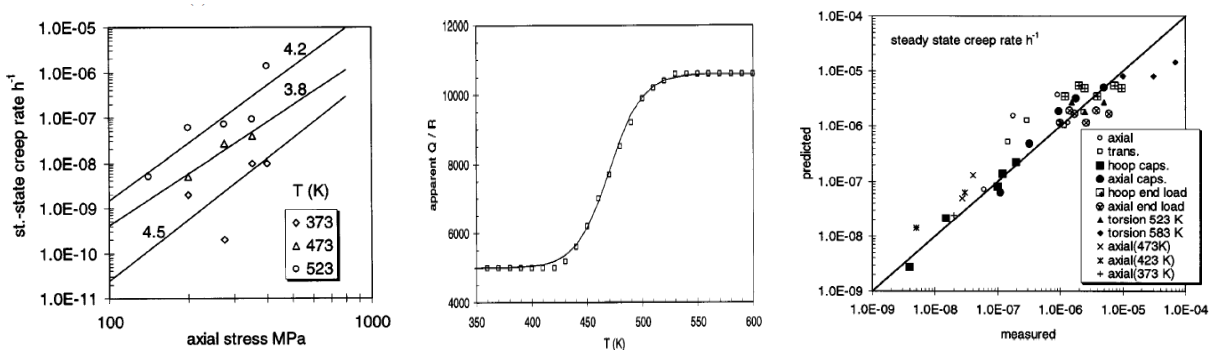

Figure 2-11: Steady creep rate measured in tension along AD of pressure tube as a function of stress imposed; dependence of apparent activation energy Q on temperature; comparison of experiments and predictions of thermal creep model implemented here (from Christodoulou et al, 2002)

We regard the framework of the thermal creep model as sound, since it is based on the possible crystallographic mechanisms responsible for creep. However, we regard the parameters of the thermal creep model as tentative, since they are specific for a Zircaloy-4 alloy, and since the validity of these parameters cannot be guaranteed beyond T=596K. In future work we will explore other databases, such as the results reported by Butcher and Donohue (1986), who measure thermal creep in-reactor, superimposed to irradiation effects. The applications of the thermal creep model are presented in Section 2.5, where we superpose all deformation mechanisms, and in Section 4, where a simulation of ballooning is presented.

2.4 Instantaneous Plasticity

Here, instantaneous plasticity is different from creep in that it is activated by imposed rates, and so the associated stress is a consequence, rather than the imposed condition as in the case of creep. Abnormal conditions in an operating nuclear reactor can be caused by temperature fluctuations associated with loss of coolant accident (LOCA) or reactivity-initiated accident (RIA). Temperature increase combined with stress leads to localized instantaneous plastic deformation, and phenomena such as ballooning and burst of cladding tubes. Irradiation-induced microstructure (e.g. interstitial clusters or dislocation loops) interacts with mobile dislocations and cause increased strain hardening and embrittlement. The effects of irradiation on flow stress and strain hardening results in yield strength increases and uniform elongation decreases with increasing irradiation dose [Maloy et al (2001), Deo et al (2008), Le Saux et al (2008), Lucas and Pelloux (2001), Gittus (1974), Onchi et al (1977), Cazalis et al (2007)]. Irradiation inhibits twinning at room temperature and above, therefore the mechanical behavior of irradiated Zircaloy is not affected by twinning [Onchi et al, 1977].

Accident conditions (e.g. low temperature in early stage transient, metal-water reaction and accumulated irradiation in a high burn-up clad may lead to brittle failure or burst. At a later stage when clad is at high temperatures (above 800^{o}C) for longer periods of time, internal pressure may increase due to fission gas release, after pellet-gap re-opening and may lead to clad failure (ballooning) via pressure controlled loading.

2.4.1 Dislocation based hardening model

The flow stress represents the stress at which dislocations are created and propagate. Because dislocation propagation relaxes stresses, this process dictates the maximum value of internal stress that the material can sustain. During plastic deformation or during irradiation the dislocation density increases, and with it the density of defects that the propagating dislocations have to overcome. As a

consequence, the flow stress increases monotonically with deformation and irradiation, a phenomenon known as hardening. Here, we implement a dislocation evolution model of hardening originally proposed by Beyerlein and Tomé (2008). We adapt the parameters of the model to experimental data of Zircaloy, and we add to it the evolution of dislocation loops associated with irradiation. The model is adjusted using experimental data obtained by Le Saux et al (2008) on Zircaloy irradiated and un-irradiated, tested in tension at different temperatures and rates. We account for the crystallographic character of plasticity by assuming that it is mediated by dislocations gliding in prismatic, basal and pyramidal planes. The total strain rate in the grain is given by the expression (2-4)

$$\dot{\varepsilon}_{ij} = \sum_s m_{ij}^s \dot{\gamma}^s = \dot{\gamma}_o \sum_s m_{ij}^s \left(\frac{m_{kl}^s \sigma_{kl}}{\tau_{thre}^s(\dot{\varepsilon}, T)} \right)^n \tag{2-15}$$

Observe that in the model the threshold stress τ_{thres}^s is a function of rate and temperature. Its dependence on dislocation density is given by Taylor law

$$\tau_{thres}^s = \alpha^f \mu b^s \sqrt{\rho^f} \tag{2-16}$$

Where the index f refers to forest dislocations (as opposed to loop) , b^s is the Burgers vector of system s, and $0.1<\alpha^f<1$ is a dislocation interaction parameter. The dislocation density evolution is composed of a storage term and an annihilation term:

$$\frac{\partial \rho^s}{\partial \gamma^s} = k_1 \sqrt{\rho^f} - k_2 \rho^f \tag{2-17}$$

The material parameters for the constitutive model are fitted against the experimental data of uniaxial tensile stress-strain reported by Le Saux et al. [2008] for non-irradiated material condition. We represent the polycrystal using 1992 crystal orientations. The initial crystallographic texture of the polycrystal is shown in Figure 2-12a and corresponds to a cladding tube. The fitted curves, along with the data reported by Le Saux et al. [2008] for 280C <T <480C and $0.01s^{-1} < \dot{\varepsilon} < 5s^{-1}$ are shown in Figure 2-12b.

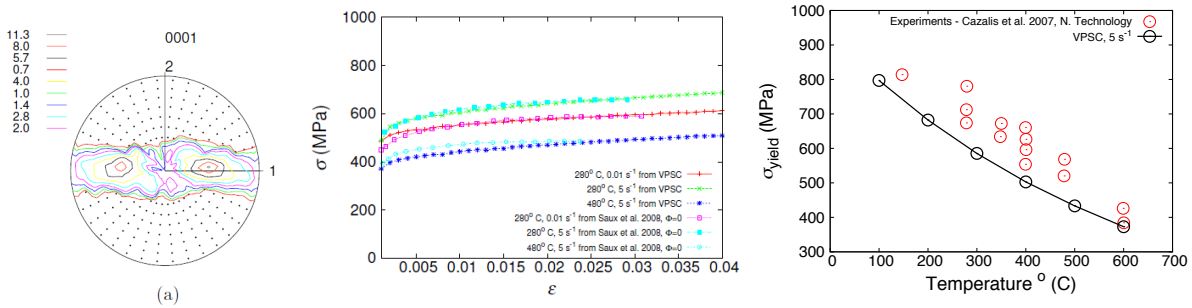

(a) (b) (c)

Figure 2-12: (a) texture of cladding tube represented using 1992 orientations extracted from EBSD measurements (1=HD, 2=AD, 3=RD); (b) predicted stress-strain response at different rate and temperatures of unirradiated tube along the axial direction, superimposed with data from Le Saux et al (2008) used for fitting hardening model parameters; (c) predicted yield stress at different temperatures for 5 s^{-1} rate, and comparison with Zircaloy-4 data of Cazalis et al (2007)

Next, we incorporate the effect of irradiation induced microstructure on hardening. The interaction of forest dislocations with immobile dislocation loops in basal and prism planes has the same dependence as in Eq. (2-16) [Arsenlis et al, 2004, 2012], except that the interaction constant α^l adopts a different value:

$$\tau^s_{thres} = \alpha^f \mu b^s \sqrt{\rho^f} + \alpha^l \mu b^s \sqrt{\sum_l N^l 2\pi r^l} \tag{2-18}$$

Here, r^l is the average loop radius and N^l is the number of loops of type l per unit volume. The evolution of loop radius and density follows from the growth model developed by [Golubov et al, 2011; Barashev et al, 2012] and its interface with VPSC described in Section 2-1 above. At any instance of an irradiation simulation the boundary conditions may be modified to allow for temperature and/or stress changes which may lead to the activation of this instantaneous plasticity mechanism. The variation of irradiation loop density with dose in each grain follows from the coupled VPSC-GROWTH model. In Fig 2-13 we present the predicted variation with dose of the total loop density in the polycrystal.

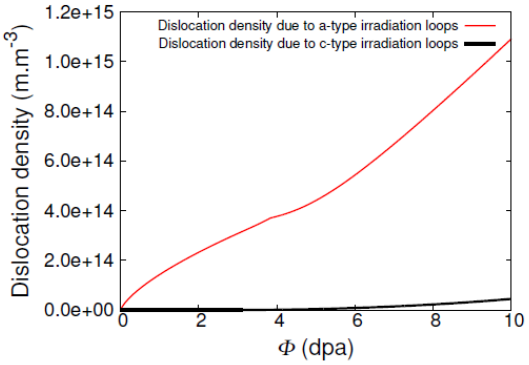

Figure 2-13: Predicted variation with dose of the total loop density in the polycrystal

In Fig. 2-14 we present simulations of tensile axial tests done at 280°C on cladding pre-irradiated to 10 dpa. Two tensile rates were considered: $\dot{\varepsilon} = 0.01s^{-1}$ (Fig 2-14a) and $\dot{\varepsilon} = 5s^{-1}$ (Fig 2-14b). It is seen that irradiation increases the flow stress by about 25%. Fig 2-14c displays the variation of yield stress versus dose for the case $\dot{\varepsilon} = 0.01s^{-1}$, and compares against experimental data reported by Le Saux et al (2008) for Zircaloy-4 irradiated to 10 dpa.

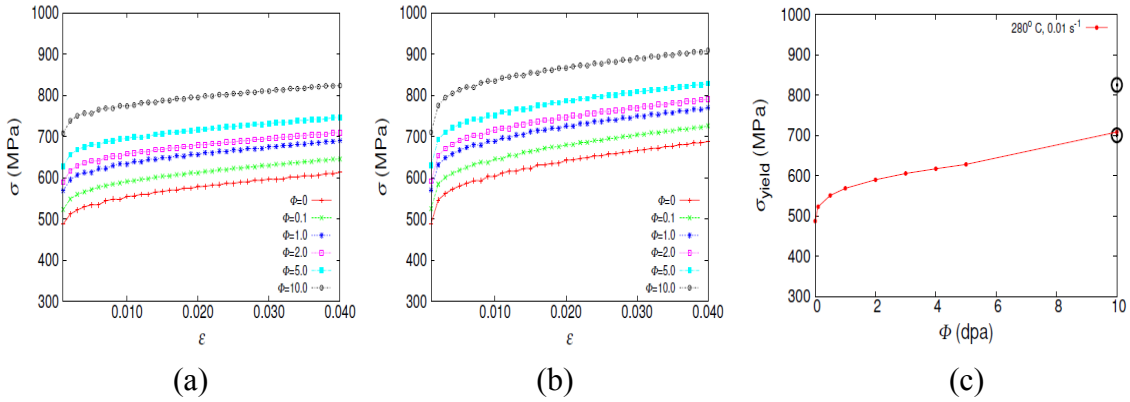

Figure 2-14: Simulations of tensile axial tests done at 280 C on cladding pre-irradiated to 10 dpa. (a) tensile rates of $\dot{\varepsilon} = 0.01s^{-1}$; (b) tensile rate of $\dot{\varepsilon} = 5s^{-1}$; (c) variation of yield stress versus dose for the case 0.01 s^{-1}, and experimental data reported by Le Saux et al (2008) for Zircaloy-4 irradiated to 10 dpa.

From the results of this section it follows that a hardening model based on the evolution of dislocation density is able to capture the stress-strain response of non-irradiated Zircaloy-4, and also the effect of irradiation induced microstructure on the flow stress of Zircaloy-4. The latter is captured through the increase of threshold stress associated with the interaction of mobile network dislocations and irradiation loops. The densities of irradiation loops are determined by using the coupled VPSC-GROWTH model. The irradiation hardening model presented in this work is able to capture strain-rate sensitivity, temperature dependence and irradiation hardening in Zircaloy-4. Given the loading conditions, burn-up, and transient time during reactor operation, the model should be able to predict the stress state in Zircoloy-4 cladding.

2.5 Standalone-VPSC Results / Superposition & Coupling

The purpose of this Section is twofold: to demonstrate the capability of VPSC for accounting for the superposition and coupling of all mechanisms described above, and to provide relatively simple benchmark cases for testing the interfacing of VPSC with the FE code PEREGRINE. As suggested by the diagram in Fig 2-1b, either irradiation creep and growth, or thermal creep, or instantaneous plasticity will prevail depending on the neutron dose, stress, and temperature, acting on the cladding tube. However, these mechanisms do not exclude each other and, what is most important, the boundary conditions on the cladding may change during operation and all the mechanisms need to be made available to the simulation code, even if their contribution is negligible for the current boundary conditions. As a consequence, the stress law for the grain will be a sum of irradiation growth (Eq 2-9), irradiation creep (Eq 2-11), thermal creep (Eq. 2-13) and instantaneous plasticity (Eq 2-15) contributions:

$$\begin{aligned}\dot{\varepsilon}_{mn}^{total} &= \frac{1}{2}\sum_{s=1}^{N_s}(\dot{N}_{i\to s}-\dot{N}_{v\to s})\rho^s(b_m^s b_n^s + b_n^s b_m^s)\\ &+\frac{1}{2}\sum_{l=1}^{N_l}(\dot{N}_{i\to l}-\dot{N}_{v\to l})\rho^l(n_m^l n_n^l + n_n^l n_m^l)\\ &+\dot{\gamma}_o(T)\sum_{s=1}^{N_s} m_{ij}^s\left(\frac{m_{kl}^s\sigma_{kl}}{\tau_{creep}^s}\right)^4 + \dot{\gamma}_o\sum_{s=1}^{N_s} m_{ij}^s\left(\frac{m_{kl}^s\sigma_{kl}}{\tau_{inst}^s(\dot{\varepsilon},T)}\right)^{20}\end{aligned} \tag{2-19}$$

The case chosen here to illustrate this capability is a pressurized cladding tube, subjected to the following piece-wise loading history:

$$\begin{aligned}&\sigma_{axial}=50MPa,\ \sigma_{hoop}=100MPa \to 0\,dpa<\Phi<13\,\text{dpa}\\ &\sigma_{axial}=100MPa,\ \sigma_{hoop}=200MPa \to 13\,dpa<\Phi<20\,\text{dpa}\\ &T=500K \to 0\,dpa<\Phi<7\,\text{dpa}\\ &T=600K \to 7dpa<\Phi<20\,\text{dpa}\end{aligned} \tag{2-20}$$

For comparison purposes, we applied such history first assuming that only irradiation, or thermal, or instantaneous plasticity is active during the run, and afterwards we made a run assuming that all three are simultaneously available. The evolution of hoop and axial strain with dose is depicted in

Fig. 2-15. The most important results is that the strain associated with coupled mechanisms is not equal to the superposition of the individual mechanisms. Second (in the scale of Figure 2-15) the irradiation effects become noticeable after breakaway growth takes place, at about 5dpa. Third, the 100K temperature jump affects little the thermal creep contribution, but the doubling of the stress makes this mechanism relevant to the total deformation. Finally, for the load conditions used here the contribution of the instantaneous plasticity mechanism is negligible.

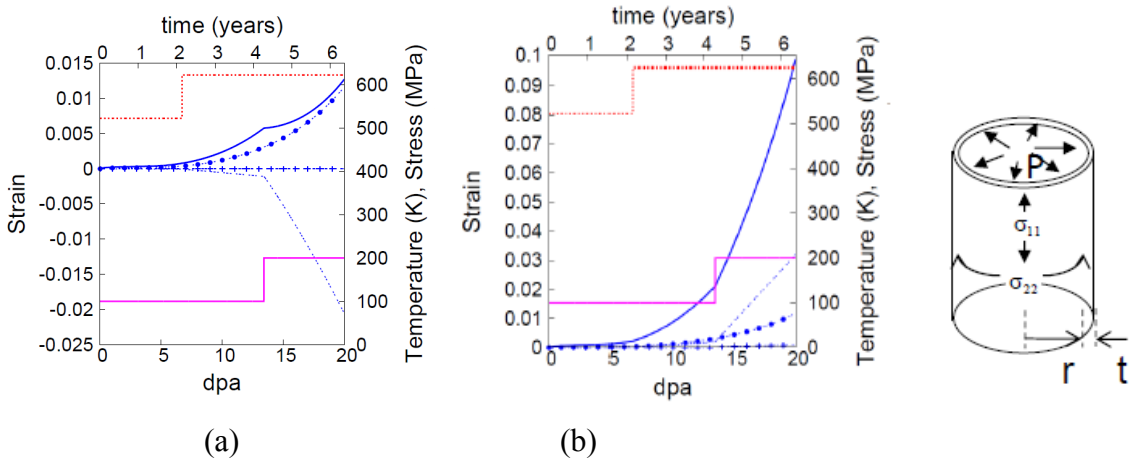

Figure 2-15: (a) hoop strain vs dose and (b) axial strain vs dose, for a cladding tube subjected to the loading history detailed in Eq (2-16). The line types identify the contribution to strain of each mechanism: ___ total, - - - thermal, ••• irradiation, ◊◊◊ instantaneous

2.6 Conclusions

We have developed a polycrystal model for irradiation growth, irradiation creep, thermal creep and instantaneous plasticity based on crystallography. Specifically, we have adapted our Visco-Plastic Self-Consistent (VPSC) code to account simultaneously for irradiation and thermal effects. Developing constitutive laws of creep and growth for cladding which explicitly incorporate the crystallographic mechanism of dislocation climb and glide, grain orientation, and interaction of grains with their surroundings constitutive a paradigm change in the way we simulate cladding behavior under irradiation. There are several advantages to adopting such approach: 1) the directionality and anisotropy of the clad response is built in the model. Deformation and stiffness can differ along each direction of the cladding tube because the model is based on tensor relations. There is no need to invoke 'effective stresses" or 'effective strain' scalar concepts; 2) the model uses information that is, in principle, accessible to measurements. Such as distribution of grain orientation (texture) or dislocation densities on different systems (basal, prism, pyramidal); 3) a conceptual difference between this model and empirical continuum laws of creep and growth is that the predictions do not rely on assume superposition of deformation contributions (creep rate plus growth rate), but instead those mechanisms are coupled at the grain level and lead to a macroscopic response of cladding that is, in general, different from the sum of the individual mechanism contributions.

3. PEREGRINE-VPSC INTERFACE

The previous section has described the approach in modeling the constitutive law of zirconium alloys using the standalone VPSC code. Unlike the engineering approach used in the current fuel performance codes, the computational cost could be high depending on the level of detail that the material property model intends to capture. However, the focus during this preliminary stage of the effort has been to develop an interface that will allow us to run cladding simulations using the crystallographic framework and models described in Section 2 within the Peregrine fuel performance code. For a single deformation mechanism, such as the process of climb and glide of dislocations in the hexagonal crystal structure of alpha-phase zirconium and its alloys, there are 18 glide systems and 4 sessile dislocation loops systems in the formulation presented in Section 2 (see Fig 2-2), and the kinetics of each slip system might depend on a number of micro-structure parameters. To consider a crystal texture which involves even dozens of grains with different orientations, the number of state variables used for modeling a single element problem is large. Figure 3-1 shows the schematic of quadrature points in a single 3-D (HEX8) element. For the HEX8 element, each element has 8 quadrature points (the computation unit to call VPSC) and to solve a fuel rod cladding deformation problem with hundreds of elements is computationally intensive.

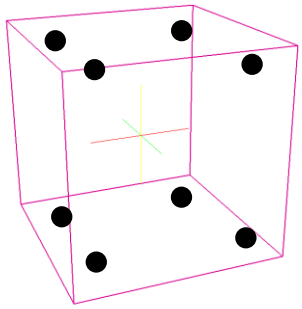

Figure 3-1 Schematic of the quadrature points in a HEX8 element

Section 3.1 describes the numerical procedure to implement the finite element framework in the MOOSE system using the Newton-Raphson method. Section 3.2 describes a procedure to reduce the number of grains for improved computational efficiency while still providing characteristic information on the texture of zirconium and its alloys. Finally, Section 3.3 gives a number of test cases to benchmark the functionality of the Peregrine-VPSC interface.

3.1 Computational Methodology

The finite element solution of a mechanical problem involves solving the weak-form equation of the mechanical equilibrium condition. In the MOOSE system, this has been formulated in an equation to minimize the residual, which is solved using Newton iteration method. To solve the nonlinear deformation problem which involves creep and plasticity, the total incremental strain at each time step is passed to a material model which would compute a trial stress tensor, and the trial stress would be used to update the weak form solution until the convergence is reached, i.e., the weak-form equilibrium equation is satisfied and the strain tensor consisting of the elastic strain and plastic strain is consistent with the applied stress. Such a computational process requires the VPSC module to compute a stress tensor for an incremental total strain.

At each time step, knowing the old stress tensor at time t, the problem is to provide an update of the trial stress at current time $t+\Delta t$ as shown in following equations.

$$\sigma_{t+\Delta t} = \sigma_t + C\Delta\varepsilon_e \tag{3-1}$$

$$\Delta\varepsilon_e = \Delta\varepsilon - \Delta\varepsilon_p \tag{3-2}$$

Where,

σ_t is the old stress tensor at time t

C is the elastic stiffness tensor of the polycrystal

$\Delta\varepsilon_e$ is the incremental elastic strain at time t

$\Delta\varepsilon$ is the total incremental strain at time t

$\Delta\varepsilon_p$ is the incremental plastic strain computed in VPSC including creep, irradiation growth, and instantaneous plasticity

The residual, R in Eq. (3-3), as a function of the trial stress is defined as the difference between the sum of the incremental elastic strain and the incremental plastic strain and the total incremental strain computed in the MOOSE system.

$$R = C^{-1}\Delta\sigma + \Delta t\dot{\varepsilon}_p - \Delta\varepsilon_t \tag{3-3}$$

Where,

$\Delta\varepsilon_t$ is the total incremental strain computed in the MOOSE system

$\Delta t\dot{\varepsilon}_p \equiv \Delta\varepsilon_p$

Newton iteration method is used to compute the trial stress.

$$\Delta\sigma_{k+1} = \Delta\sigma_k - \frac{\partial R}{\partial\Delta\sigma_k} R(\Delta\sigma_k) \tag{3-4}$$

Subscript k represents the k_{th} iteration in the sub-Newton iteration loop to compute trial stress. The convergence of the numerical method depends on either of the following error is lower than prescribed tolerance.

$$e_1 = \left|\Delta\varepsilon_t - \Delta\varepsilon_p(\sigma_{tr}) - \Delta\varepsilon_e(\sigma_{tr})\right| \tag{3-5}$$

$$e_2 = \left|\Delta\varepsilon_t - \Delta\varepsilon_p(\sigma_{tr}) - \Delta\varepsilon_e(\sigma_{tr})\right| / \left|\Delta\varepsilon_t\right| \tag{3-6}$$

$$e_3 = \left|\Delta\varepsilon_{t,k} - \Delta\varepsilon_{p,k}(\sigma_{tr,k}) - \Delta\varepsilon_{e,k}(\sigma_{tr,k})\right| / \left|\Delta\varepsilon_{t,1} - \Delta\varepsilon_{p,1}(\sigma_{tr,1}) - \Delta\varepsilon_{e,1}(\sigma_{tr,1})\right| \tag{3-7}$$

Where,

σ_{tr} is the trial stress computed in VPSC,

$\Delta\varepsilon_t$ is the total incremental strain,

$\Delta\varepsilon_e$ is the incremental elastic strain,

$\Delta\varepsilon_p$ is the incremental plastic strain,

Subscript k in the subscript represents the k_{th} iteration in the Newton iteration loop to compute the trial stress.

An in depth description of the basic computational method of coupling VPSC to a finite element code can be found elsewhere (Segurado, 2012). To distinguish this iteration method from the iteration method used in the MOOSE system solving the weak-form equation, we also call this sub-Newton iteration indicating that this iteration is embedded in the nonlinear iteration loop of the MOOSE system. Figure 3-2 shows the schematic of coupling between the MOOSE Solid Mechanics module, the finite element kernel in the MOOSE system that solves the weak-form mechanical equilibrium equation, and the VPSC module.

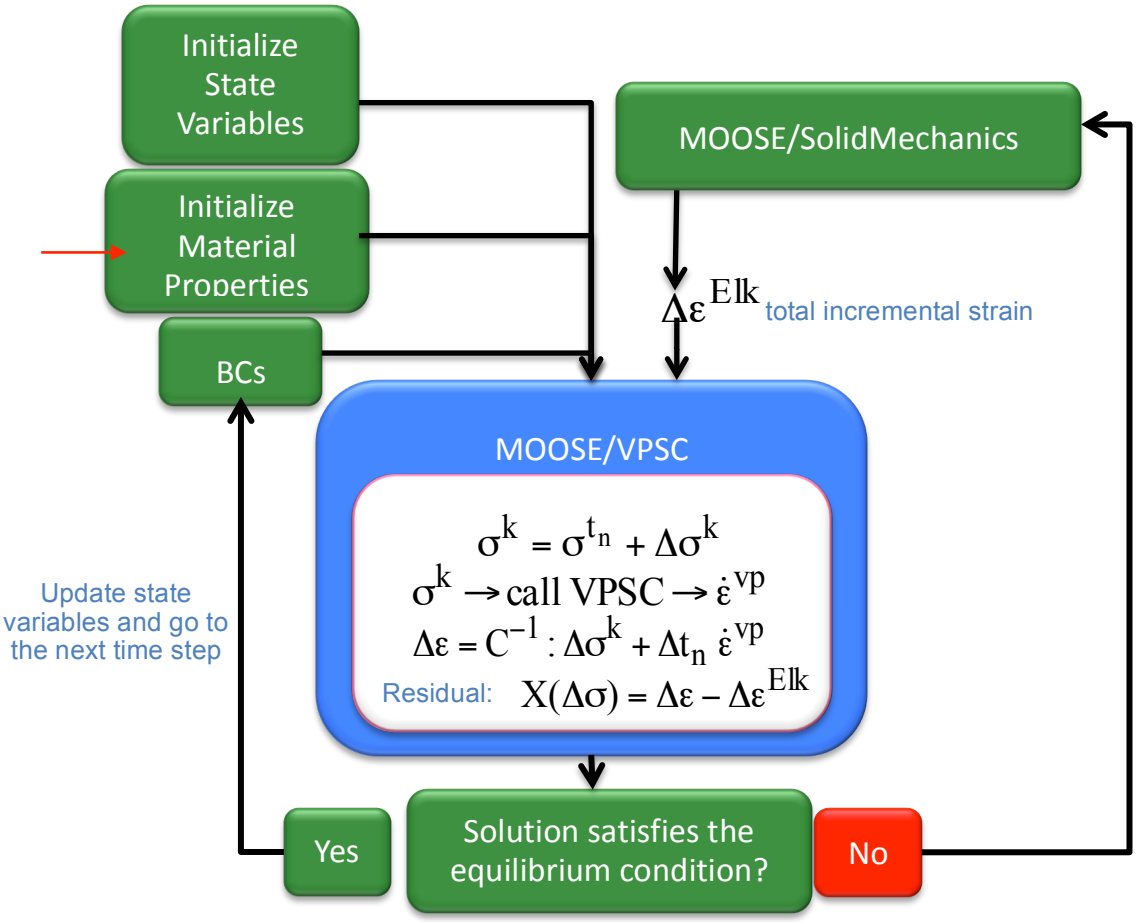

Figure 3-2 Schematic of the numerical method of coupling VPSC and Peregrine

The material property is represented in each integration point in the finite element code. The VPSC module which computes the viscoplastic strain for given stress state needs to keep track of all the state variables including plastic strain, orientation, activity and activation stress for each slip system in each grain, dislocation density on each slip system, etc. Those state variables at each integration point are stored in the MOOSE system and are shared with VPSC module; updating the state variables are performed in the Peregrine-VPSC interface when the sub-iteration gets converged at each time step.

3.2 Representative Zirconium alloy texture (EBSD and texture reduction)

In this Section we discuss the concept of crystallographic texture, its relevance in determining anisotropic response, and how we represent texture in our crystallographic model.

VPSC is a polycrystal plasticity formalism, based on representing the material as a collection of Zr-alloy crystal orientations (grains) chosen to reproduce the experimentally measured texture. VPSC is an 'effective medium' formalism where each of those grains are assumed to have ellipsoidal shape, to be embedded in an effective medium with the average mechanical properties of the polycrystal. The mechanical stress-strain response of the grain is a consequence of the interaction with the medium. The average over all the grains provides the mechanical response and properties of the medium in a self-consistent fashion.

In the specific case of cladding tube the constituent grains have hexagonal symmetry, characterized by a unit cell with the c-axis perpendicular to the compact basal plane (Figure 2-4). Hexagonal

crystals are usually highly anisotropic, meaning that the properties along the c-axis or perpendicular to it are very different. A specific example that applies to our problem is: interstitial clusters diffuse only along the basal plane and lead to formation of interstitial loops in the prism planes, while excess vacancies form loops on the basal planes. This configuration of loops is responsible for negative growth along c-axis and positive growth perpendicular to it. The extrusion forming of the cladding tube orients the c-axis of these crystals mostly in the Radial-Hoop plane (Fig. 2-4). As a consequence, prism planes are oriented mostly along the Axial directions, which explains the positive axial growth observed in cladding.

As mentioned in Section 2.1.2, the texture is represented by a discrete number of crystals (grains) with assigned orientations (typically from 1000 to 3000), and the Polycrystal Plasticity code VPSC uses this ensemble as the material representation. Different alloys and different manufacturing routes can lead to different textures which in turn lead to different creep and growth behavior during irradiation. As a consequence, introducing the texture explicitly in the simulation leads to differences in the macroscopic response, although the constitutive response of the constituent grains is the same. Internally, VPSC keeps track of the stress, strain, crystal orientation, activity and activation stress for each slip system in each individual grain, dislocation density on each slip system, etc. In computational terms this requires us to keep track of several magnitudes and state variables associated with each grain, and to update them after each simulation step takes place. While this *modus operandi* is feasible when performing stand-alone runs of the VPSC code, it becomes computationally onerous when VPSC is used to describe the mechanical response of each integration point in the FE simulation. The reason is that now one full polycrystal is assigned and its internal state updated for each integration point, which multiplies by many orders of magnitude the running times, memory storage requirements, and internal variable swaps between the material subroutine (VPSC) and the boundary problem solver (PEREGRINE). As a consequence, the strategy chosen here to optimize running times of PEREGRINE is to reduce to a minimum the number of orientations used to represent the texture, while preserving the accuracy of the response predicted by VPSC.

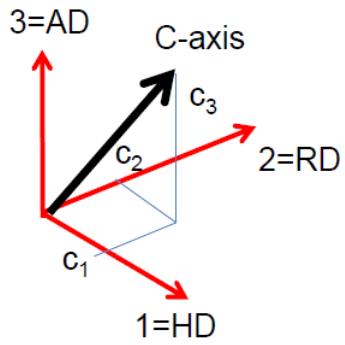

The role of texture in altering the macroscopic response is well recognized and it has been introduced in the continuum models of creep and growth through the Kearns factors. The latter utilize a quantitative measure of the basal component (c-axis orientation) in the texture to 'weight' the directional response of the cladding tube. If $\hat{c} = (c_1, c_2, c_3)$ are the components of the c-axis with respect to tube axes, the Kearns factors are defined as the average of the projections of the c-axis (direction cosines) of the N_g grains that define the polycrystal.

$$f_i = \frac{1}{N_g} \sum_{g=1}^{N_g} (c_i)^2 \qquad (i = 1,2,3) \tag{3-8}$$

In the particular case of the typical cladding tube texture used in this work, constituted by 1944 grains, the Kearns factors are 0.424 (hoop), 0.547 (radial) and 0.028 (axial) (see Table 3-1). Our modeling strategy consisted in generating textures having approximately the same Kearns factors but a much reduced number of grains, and to compute irradiation creep and growth strains for each of those textures. Figure 3-3 depicts the original texture and 3 reduced textures composed by 100, 4 and 2 grains. As it turns out, the results of the 100-grain texture are nearly indistinguishable from the

ones of the 1944 grain texture, while the 4 grain texture gives deviations of about 5% and the 2-grain texture gives deviations of about 20% in predicted strain vs dose. As a consequence, the 4-grain texture represents an acceptable compromise between accuracy and computation time, and is the one adopted in what follows for interfacing VPSC with PEREGRINE.

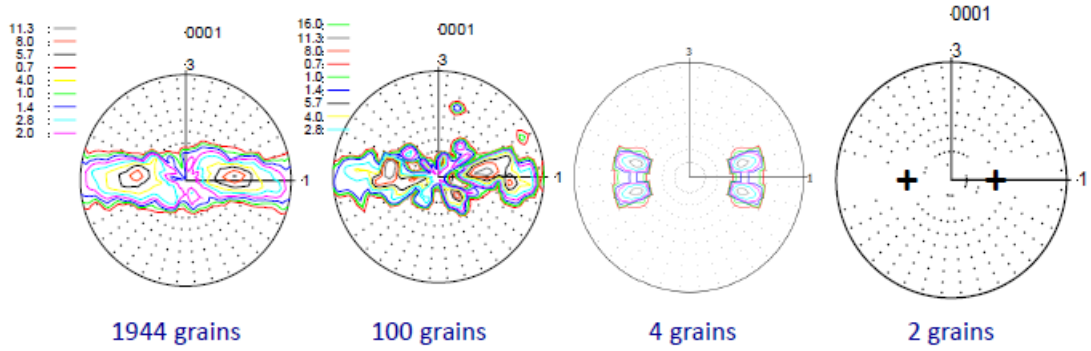

Figure 3-3 Cladding tube texture representation using different number of orientations

Table 3-1 Kearns factor for different numbers of reduced grains representing the Zirconium alloy texture. X = direction 1 (hoop), Y = direction 2 (radial), Z = direction 3 (axial)

Number of grains	fx	fy	fz
1944	0.4244	0.5472	0.0284
100	0.4178	0.5516	0.0306
4	0.4244	0.5472	0.0284
2	0.3290	0.6710	0.0

3.3 Benchmark cases

A number of benchmark cases were used to test the functionality of Peregrine-VPSC. The results of the test cases have been compared to standalone VPSC results. Table 3-2 below lists all the benchmark cases used for the tests. A single 3-D eight-node element has been used for all the test cases.

Table 3-2 List of test cases for benchmarking Peregrine-VPSC

#	Description	Temperature, K	Stress, MPa (Direction)	Texture
1	Thermal creep	523	10 (Y)	(0, 0, 0)[a]
2	Instantaneous plasticity	523	100 (Y)	four-grain
3	Irradiation creep and growth[b]	523	1 (Y)	(0, 0, 0)
4	Creep with large deformation	1073	200 (X)	four-grain

[a] The texture file describes the fraction of crystals with basal poles in certain direction in terms of Euler angles in three consecutive rotations: a) The first angle is the angle of rotation around the axis Z; b) The second angle is the angle of rotation around the axis X in the new coordinate system; and c) The third angle is the angle around the axis Z in the new coordinate system.

[b] Dose rate = 1.0e-7 dpa/sec

The schematic of the basal poles are shown in Figure 3-1. The orientation of the four grains, assuming each grain is equally weighted in its crystallographic direction, is described using three Euler angles in Table 3-3.

Table 3-3 Four-grain texture described using Euler angles

	First Euler angle (degree)	Second Euler angle (degree)	Third Euler angle (degree)
Grain 1	138.63	80.30	0.00
Grain 2	138.63	99.70	0.00
Grain 3	221.37	80.30	0.00
Grain 4	221.37	99.70	0.00

The test case #1 tests the thermal creep model under a constant stress, and the results of the comparison between Peregrine-VPSC and standalone VPSC are shown in Figure 3-4.

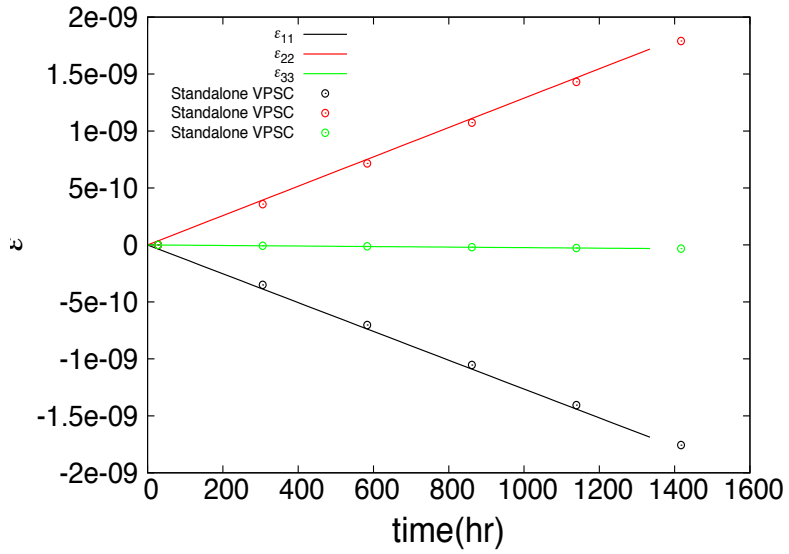

Figure 3-4 Thermal strain at 523 K for single crystal with 10 MPa along direction Y (symbols are results of standalone VPSC and solid lines are results of Peregrine-VPSC)

The test case #2 tests the functionality of the instantaneous plasticity model in the VPSC module, and the results of the comparison between Peregrine-VPSC and standalone VPSC are shown in Figure 3-5.

The test case #3 tests the functionality of the irradiation growth and creep model in the VPSC module, and the results of the comparison between Peregrine-VPSC and standalone VPSC are shown in Figure 3-6. Peregrine-VPSC can predict the irradiation growth strain in the same magnitude as the standalone VPSC. However, the result has shown the mismatch between Peregrine-VPSC and standalone VPSC results. It was found that the input condition to call the irradiation growth subroutine in Peregrine-VPSC is not exactly same as that in the standalone VPSC; further investigations are needed to resolve the discrepancy.

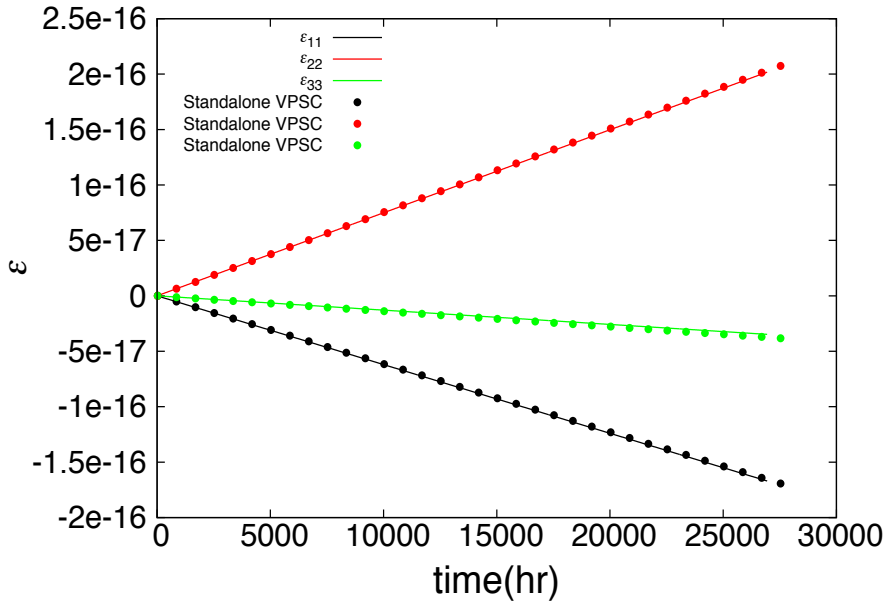

Figure 3-5 Plastic strain at 523 K for four-grain polycrystal with 100 MPa along direction Y (symbols are results of standalone VPSC and solid lines are results of Peregrine-VPSC)

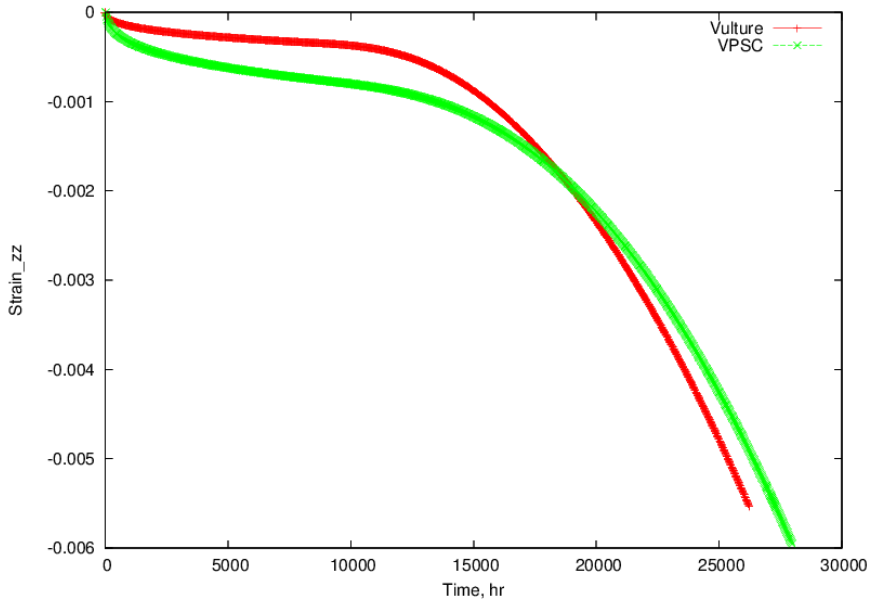

Figure 3-6 Comparison between Peregrine-VPSC (red curve) and standalone VPSC (green curve) on the irradiation growth of a single crystal

The test case #4 was prepared to test the modeling of large deformation using Peregrine-VPSC. The results of the comparison between Peregrine-VPSC and standalone VPSC shown in Figure 3-7 shows the exact match between Peregrine-VPSC and standalone VPSC on strain calculations. Results in Figure 3-8 show that the displacement, once converted to true strain, agrees with the strain output in Peregrine-VPSC.

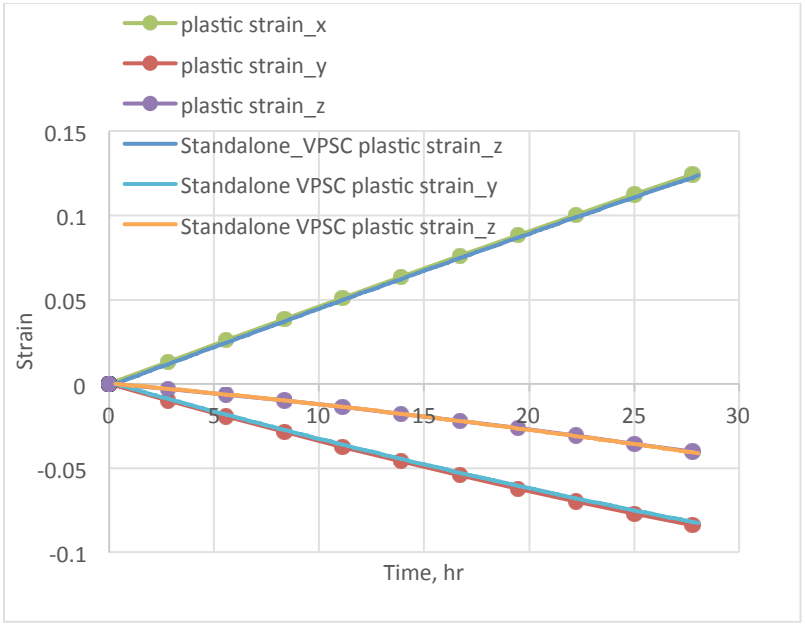

Figure 3-7 Comparison between Peregrine-VPSC and standalone VPSC on modeling high temperature creep of four-grain polycrystal

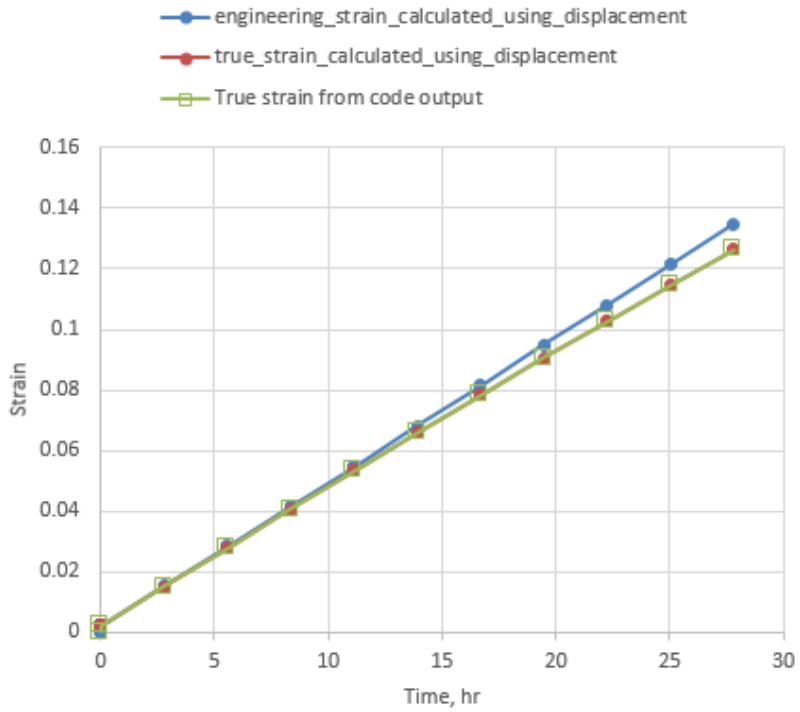

Figure 3-8 Comparison between the true strain from code output and the true strain computed using displacement

3.4 Conclusion

A numerical Newton Raphson method to link the mechanism based microstructure model to the finite element solution has been implemented in the multiphysics fuel code Peregrine. It computes trial stress for given input of total strain. A procedure of reducing the number of grains to provide representative crystallographic texture was developed to reduce the computation time.

The benchmark results have demonstrated the successful coupling between Peregrine code and the VPSC module. When linked in the finite element framework, the deformation process during the in-reactor normal operation that involves the creep, irradiation growth, and plasticity can be simulated using the VPSC material model. The reduced number of grains in representing the crystallographic texture has provided an efficient method of running Peregrine-VPSC. One of these test cases has also demonstrated the capability of modeling large deformation using Peregrine-VPSC, which is of interest to model the clad response in accident conditions.

4. DEMONSTRATION OF VPSC IN PEREGRINE

This section presents the results of testing the mechanism-based microstructure model on irradiation growth and the demonstration of the capability of Peregrine-VPSC on calculating clad mechanical response at high temperature representative of loss of coolant accident (LOCA) conditions. Section 4.1 describes the comparison between the mechanism based irradiation growth model and an empirical clad elongation model based on regression analysis of in-reactor measurement data to account for microstructure texture effects on irradiation growth behavior. Section 4.2 describes the results of running Peregrine-VPSC to model the large deformation at high temperatures to demonstrate the code's capability of modeling clad ballooning in the postulated LOCA condition.

4.1 Irradiation Growth

Calculation of fuel rod elongation during irradiation is an important function of engineering scale fuel performance codes. Figure 4-1 provides an example of the fuel rod elongation by irradiation growth observed in a variety of fuel rods (Alvis and Montgomery, 2004). The data extends to fast neutron fluence levels approaching 1.5×10^{22} n/cm^2 at energy levels above 1 MeV. The database shown in Figure 4-1 is composed of fuel rods operated under a variety of irradiation conditions and cladding material obtained from vastly different manufacturing processes. As a result, significant scatter in the data is observed when compared to empirical modeling approaches like that derived by Franklin, et al.

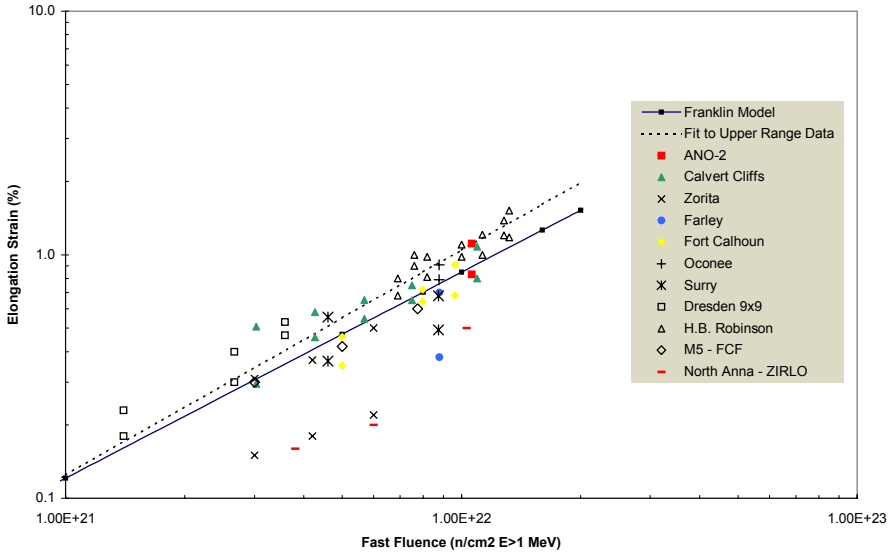

Figure 4-1 Typical elongation strain data for LWR fuel rods as a function of fast neutron fluence (Alvis and Montgomery, 2004)

The Franklin model of cladding irradiation growth shown in Figure 4-1 was derived from an extensive irradiation and post-irradiation examination program performed in the 1970's to obtain data on Zircaloy-4 cladding axial elongation, circumferential creep, ovalization, and ridging. Regression analysis of the data was used to determine the important variables that influenced the cladding deformation mode. Also, these regression analysis results have been used in several fuel performance codes. Even today, the program sponsored by EPRI is one of the most comprehensive cladding deformation examination database available in the literature to qualify or compare constitutive models.

4.1.1 Texture Effect in Empirical Models

Franklin performed the regression analysis on the 72 LWR rods (60 fuel rods and 12 non-fueled rods) from the CE irradiation program and 65 characterized rods from Westinghouse irradiation program. Several empirical models were developed correlating the fractional length change with the fast neutron fluence and a number of design and material parameters. The correlation that has included the texture effect can be summarized in the following equation:

$$\frac{\Delta L}{L} = A(\phi t)^m [\cos(\theta_{\max})]^j \sigma_y^k \tag{4-1}$$

Where

ΔL is the rod length change (m)
L is the rod length (m)
ϕ is fast neutron flux (n/cm^2/sec), E > 1 MeV
θ_{max} is the angle between the maximum intensity of basal pole and the radial direction in the radial-circumferential plane (degree)
σ_y is clad yield stress (MPa)

A, m, k, and j are fitting constants determined by regression analysis.

The cladding tubes used in the irradiation test programs were provided by different manufacturing processes. The test specimens have variations in the heat treatment, chemical composions, grain size, texure, etc. Therefore, the regression analysis performed using Equation 4-1 could not have sufficiently reflected the differences in the material parameters. In the regression analysis performed by Franklin, a single parameter was chosen to represent the material microstructure for the tubes in the database. This parameter, θ_{max}, is defined as the angle between the maximum intensity of the basal pole and the radial direction in the radial-circumferential plane.

The reported $\cos(\theta_{max})$ of the characterized test rods ranges from 0.6427 to 0.8746 (See Table A-1 and Table A-2 in Appendix). The correlation (Eq. (4-2)) shows that the fractional length increase is proportional to $\cos(\theta_{max})^{1.75}$ when only fast fluence and $\cos(\theta_{max})$ are used as independent variables; the fractional length increase is proportional to $\cos(\theta_{max})^{2.44}$ when the clad hoop stress is also used as an independent variable in the correlation (Franklin, 1982).

$$\frac{\Delta L}{L} = 3.69e-17(\phi t)^{0.655}[\cos(\theta_{\max})]^{1.75} \tag{4-2}$$

The data reported by Franklin were reviewed and a regression analysis to include the effect of yield stress was also performed. Eq. (4-1) can be converted to the following equation to perform the linear regression analysis.

$$\ln\frac{\Delta L}{L} = b + m\ln(\phi t) + j\ln\cos(\theta_{\max}) + k\ln\sigma_y \tag{4-3}$$

The results of the fitting parameters are provided in Table 4-1.

Table 4-1 Fitting parameters in the irradiation growth model determined from regression analysis

	k	*j*	*m*	*b*
All rods	0.725	1.822	0.853	-4.691
Non-fueled rods	1.118	1.629	0.663	-5.662

The new fitting results show that the irradiation growth strain is proportional to $\cos(\theta_{max})^{1.821}$ by using all the characterized rods (fuel rods and non-fueled rods) or to $\cos(\theta_{max})^{1.629}$ by using only the

non-fueled rods. Since the exponent 1.75 in Eq. (4-2) is close to the new fitting exponent 1.822 and 1.629, the Eq. (4-2) is used to compare to the analysis of texture effects using VPSC.

4.1.2 VPSC Analysis Using Two Grain Representation

The material characterization information in the elongation data (Franklin, 1982) did not provide sufficient details, but only the θ_{max} or $\cos^2(\theta_{max})$ (the Kearns factor in the radial direction). Therefore, the texture effect on the irradiation growth was examined using the two-grain texture representation without basal poles in the axial direction. By varying the orientation of each grain, different texture is created for the simulation. Table 4-2 shows the input crystallographic parameters for the different texture used for the simulation.

Table 4-2 Input crystallographic parameters for different texture

θ_{max} (degree)	fr[a]	Euler angles (degree) of rotation
30	0.7500	(150, 90, 0) (210, 90,0)
35	0.6710	(145, 90, 0) (215, 90, 0)
40	0.5868	(140, 90, 0) (220, 90, 0)
45	0.5000	(135, 90, 0) (225, 90, 0)
50	0.4132	(130, 90, 0) (230, 90, 0)

[a] fraction of basal poles in radial direction

Different initial dislocation densities (ρ_d=1.67e11/m^2 and ρ_d=1.67e12/m^2 respectively) are used to represent cladding alloys with different cold work factors. At the irradiation dose of 5 dpa (neutron dose equivalent to a fast fluence of ~1x10^{22} n/cm^2), all irradiation growth strains are normalized by the growth strain computed at θ_{max}=30^o. A comparison between the engineering model reported by Franklin and VPSC calculations is shown in the Figure 4-2 below. It appears that the two approaches only have agreement in a limited range of θ_{max} with higher values of $\cos(\theta_{max})$, and a large discrepancy is noticeable at lower values of $\cos(\theta_{max})$ or larger θ_{max} for the zirconium alloys with different degree of cold work as represented by different initial dislocation densities.

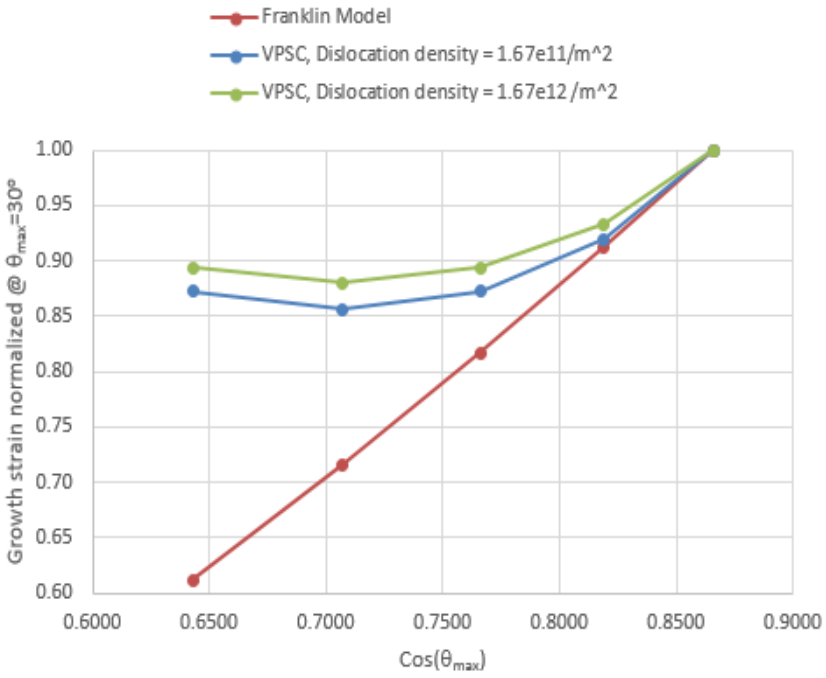

Figure 4-2 Comparison between the engineering model and VPSC results in modeling irradiation growth at different θ_{max} at 5 dpa

A theoretical interpretation on the irradiation growth behavior calculated by VPSC is that the grain-grain interaction could be stronger at lower values of θ_{max}, which may contribute to the multiplication of dislocations, climb of dislocations and, as a consequence, to the irradiation growth. The discrepancy of the results between the mechanism based model and the empirical model highlights the difference in the two modeling approaches, and challenges the applicability of the empirical correlation under certain conditions. The result indicate the power law function of $\cos(\theta_{max})$ in the empirical correlation of irradiation growth model may not be applicable, which however could not be captured in the development of empirical models which are based on certain assumptions. A careful examination of the measurement data has shown that among all the non-fueled rods, only three out of the twelve non-fueled rods have $\cos(\theta_{max}) = 0.6427$; and all the other cases have $\cos(\theta_{max})$ in the values of 0.848 and 0.8746. The measured clad elongation of the fuel rods however may have included some effects due to the pellet-clad interaction. Those limitations in measurements could also have limited the fidelity of the empirical models.

The literature includes several papers that describe the texture effects in terms of the fraction of basal poles in the axial directions (Adamson, 1982; Hagrman, 1981) which could provide useful information for the further testing of the irradiation growth model in VPSC.

4.2 High Temperature Creep Test

During a postulated LOCA, the conditions external to the fuel rod lead to significant heat up of the cladding and decrease in coolant pressure. Cladding temperatures can range from 600°C to 1200°C, depending on a variety of factors. Under these conditions, thermal creep and plastic deformation of the cladding can lead to large strain accumulation, a phenomenon called ballooning. Clad ballooning is important during a LOCA as the cladding expansion will cause reduction and blockage of the coolant channel, adversely impacting the coolant flow and heat transfer conditions. Transient fuel behavior modeling is to calculate the cladding deformation during ballooning in order to account for the impact of irradiation on rod internal pressure and fuel stored energy. Several empirical

correlations for the thermal creep rate of zirconium alloys has been obtained from experimental data. These models have been used to estimate the burst stress and burst strain data as shown by Jahingir et al. using Falcon (Jahingir, 2005).

4.2.1 Creep Properties at High Temperatures

As described in Section 2.3, the current material parameters for the creep model in VPSC for zirconium alloys are benchmarked against measurement up to 596 K. At high temperatures, the microstructure material model parameters need to be re-calibrated. We are only aware of the survey done by Wang et al (2013) for thermal creep data of unirradiated Zircaloy-4 at high temperature, and the creep magnitudes are similar to the ones that we predict with our model if we adjust the value of the dislocation activation energy with temperature. As a consequence, for the purpose of this demonstration, the approach taken for modeling viscoplastic deformations at high temperature is to make an ad-hoc change in the activation energy. Creep rates calculated by the standalone-VPSC have been compared to the creep rates by other models (Limbäck, 1996; Erbacher, 1982) to provide a reference for the calibration. Figure 4-3 plots the creep rates under a hoop stress of 200 MPa at 1073 K and 673 K using different activation energies using VPSC and creep rates as a function of temperature using engineering models. Figure 4-4 plots the fitting of creep rate to the activation energy at two different temperatures. In the demonstration problem, Q/R=18000 K is used to replace the parameter Q/R=10000 at T=596 K in the creep model described in Section 2.

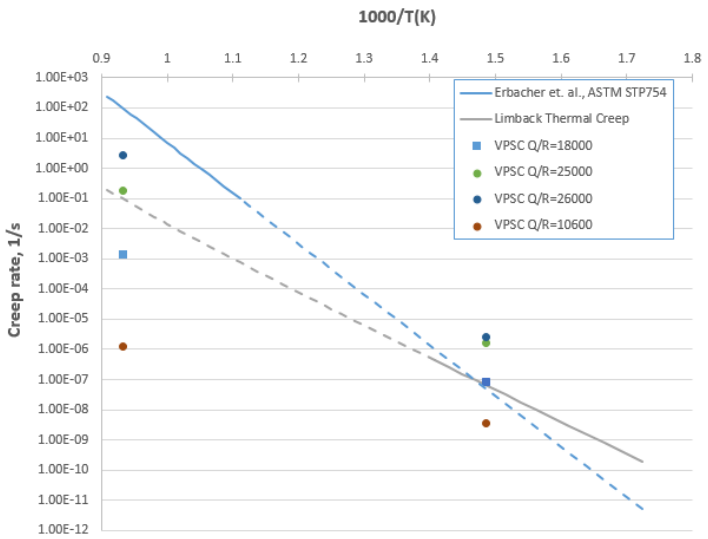

Figure 4-3 VPSC Creep rates under hoop stress of 200 MPa at different activation energies in comparison with other thermal creep models (solid curves represent applicable ranges of models; dotted curves are extrapolated calculations).

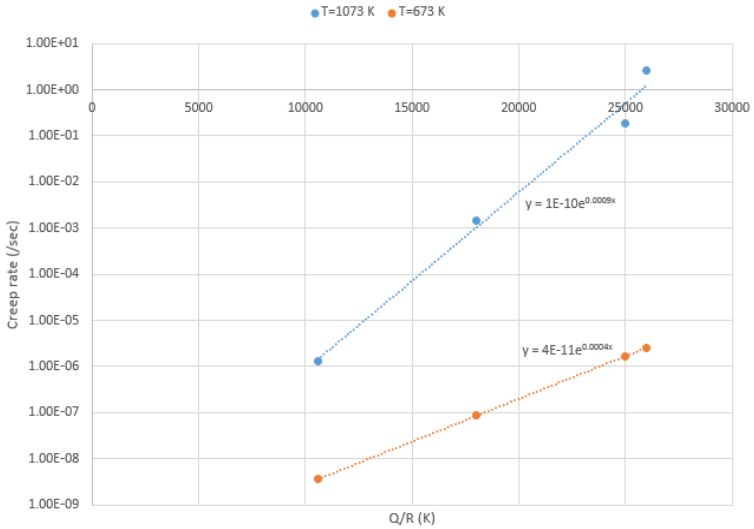

Figure 4-4 VPSC Creep rates under a hoop stress of 200 MPa versus activation energy at different temperatures

It should be noted that the anisotropic creep deformation at high temperatures was discussed by (Massih, 2011 and Erbacher, 1982). The anisotropic creep can be addressed in the VPSC model since it has accounted for the crystallographic texture which has been missing in the empirical isotropic high temperature creep models in the traditional fuel codes.

4.2.2 Peregrine-VPSC Analysis of High Temperature Creep

A test case to model a segment of clad tube axially constrained was prepared to test the capability of modeling the large deformation to simulate the clad ballooning in a Loss-of-Coolant-Accident condition using Peregrine-VPSC. The key input parameters are provided in Table 4.3 and Figure 4-5:

Table 4-3 Input parameters for the high temperature creep test case

Parameter	Unit	Value
Number of elements	-	5
Element type	-	QUAD4 axisymmetric
Internal Pressure	MPa	20
External Pressure	MPa	0.0
Texture	-	Four-grain
Time dependent average temperature	K	810 – 1073 K
Simulation time	hr	0.12[a]
Axial temperature profile	-	Peak at the mid-height position; peak to average ratio=1.012
Time steps	-	50

[a] including 0.1 hr temperature ramp and 0.02 hr high temperature hold

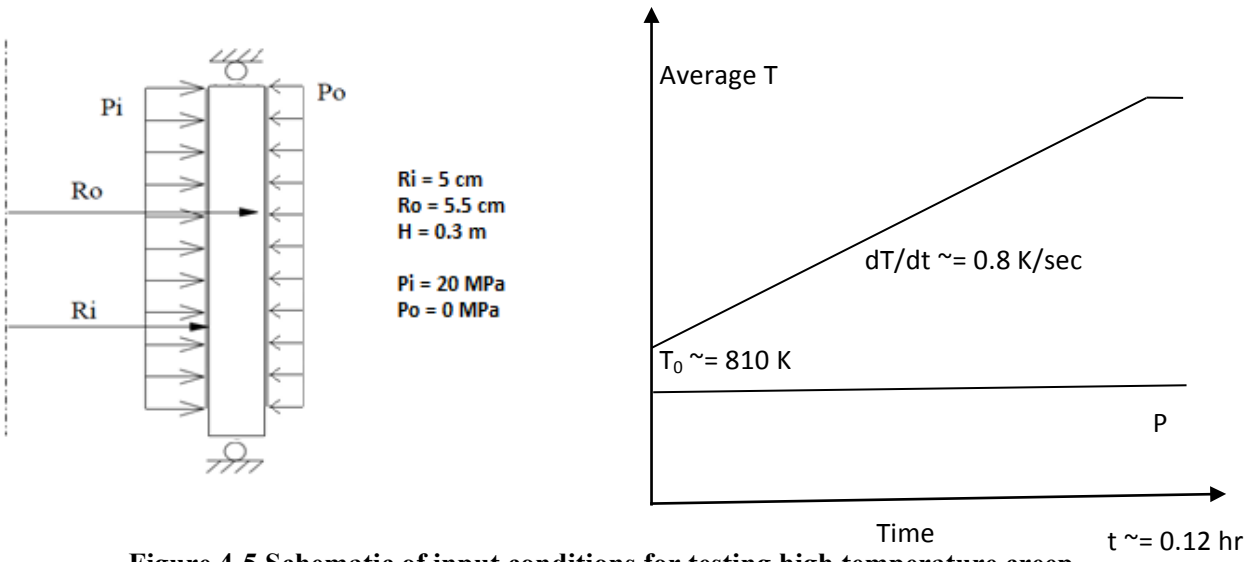

Figure 4-5 Schematic of input conditions for testing high temperature creep

Results of the total strain computed using Peregrine-VPSC are shown in Figure 4-6 below. Figure 4-7 shows the deformed geometry at the end of simulation under the imposed axial temperature profile. Figure 4-8 shows the comparison of the hoop strain between the mid-height element with the largest deformation and the top element with relatively smaller deformation.

The large deformation can be simulated due to accumulated creep strains in the whole segment of the cladding tube under rod internal pressure. The initial difference in deformation between the mid-height element with higher temperature and top/bottom element with lower temperature is small; the major difference is due to different creep rates at different temperatures. When the deformation becomes large (hoop strain > 5%), both the temperature and the deformed geometry contribute to the deformation rate. This result is consistent with experimental data obtained by Erbacher, et al. who demonstrated that azimuthal temperature variation of ~25 K is sufficient to reduce the circumferential average ballooning strain by a factor of 2.

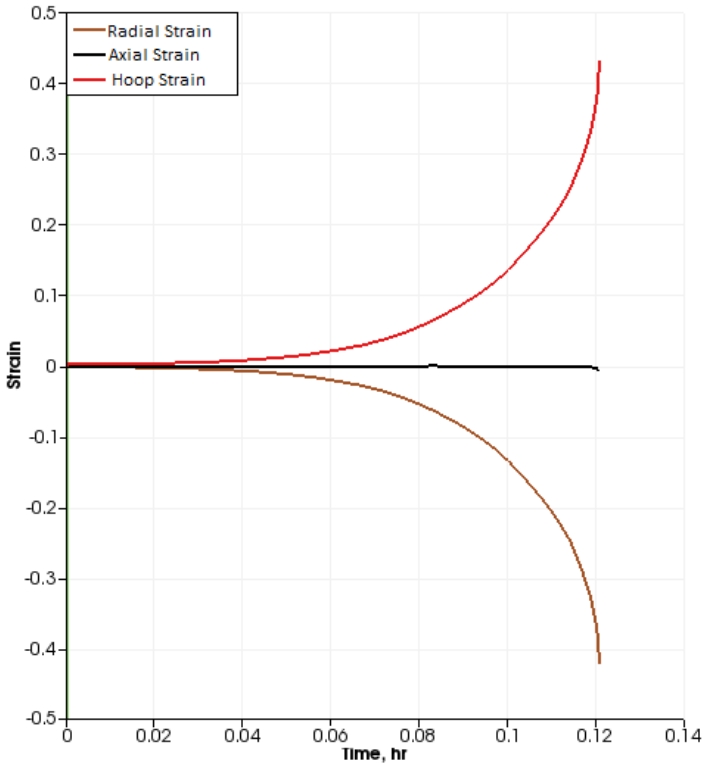

Figure 4-6 Total strains versus time at the mid-height element

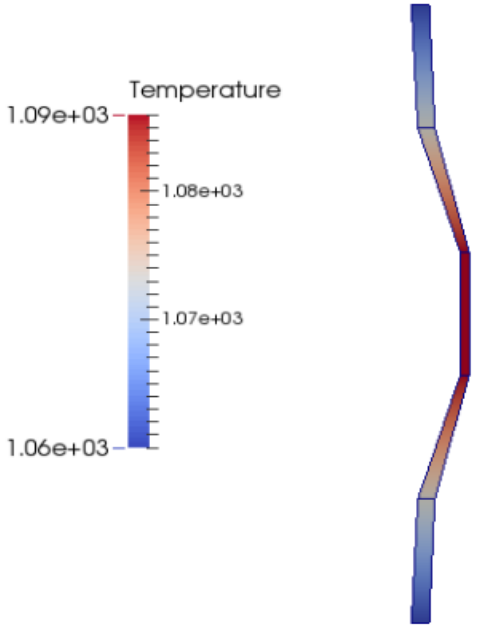

Figure 4-7 Temperature profile and deformed geometry at the end of simulation (Aspect ratio scaled 20x)

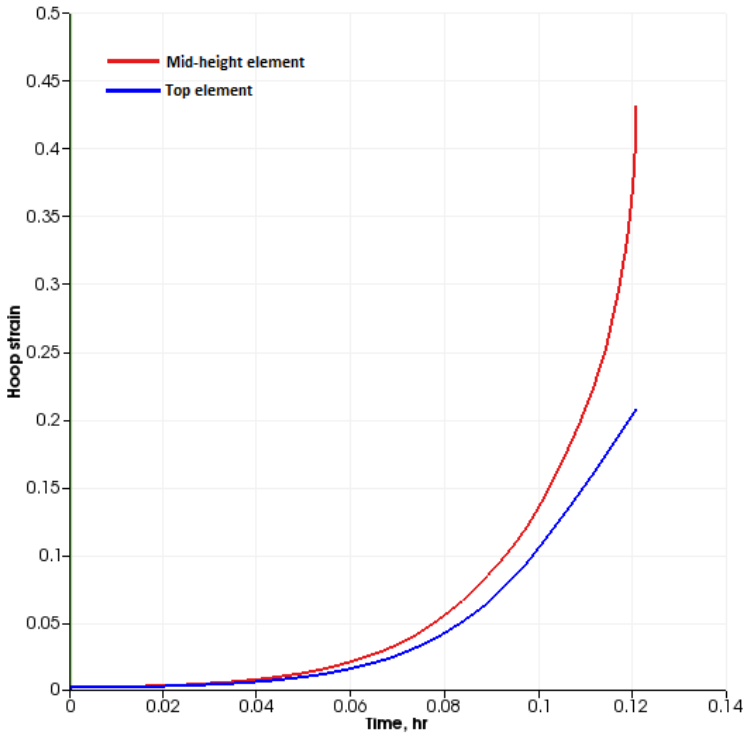

Figure 4-8 Comparison of hoop strain between the mid-height element and the top element

The higher temperature at the mid-height element promotes a higher creep rate which results in more localized wall thinning. The mid-height segment with higher temperature (1086 K @ 0.12 hr) has more than 40% cladding wall thickness reduction as compared to the 20% cladding wall thickness reduction at the top and bottom segments with relatively lower temperature (1060-1073 K @ 0.12 hr). Under constant pressure load, the true hoop stress increases as a result of wall thinning which in turn contributes to a higher creep rate. This case has demonstrated that the temperature difference (<30 K) could cause the large localized deformation to simulate the clad ballooning.

4.3 Conclusions

The results have demonstrated the capability of modeling irradiation growth using the mechanism-based microstructure model and modeling of large deformation at high temperatures using Peregrine-VPSC. Comparison of the empirical model equations and the reduced texture results using two grains has highlighted the differences between the microstructure model and the empirical correlation. The result suggests that the mechanism based microstructure model could provide more information, which cannot be provided in the empirical modeling approach. The test results on modeling high temperature creep to simulate the large clad deformation in a postulated LOCA condition has shown that under imposed axial temperature profile, the localized clad thinning (or ballooning) can be simulated using Peregrine-VPSC.

5. CONCLUSIONS

The US DOE's Consortium for Advanced Simulation of Light Water Reactors (CASL) program is developing multiphysics, multi-dimensional modeling and analysis capabilities to assess safety margins and the impact of plant operation on fuel rod behavior. Integral to this endeavor is the research and development activities to expand the mechanistic cladding deformation modeling that builds on the recent advances in computational material science.

Several activities have started to address the needed capabilities for advanced modeling of fuel behavior during normal, operational transients, and accident events. One of these efforts is the expansion and incorporation of a microstructure-based deformation model using the Visco-Plastic Self-Consistent (VPSC) approach into Peregrine to calculate thermal and irradiation-induced creep, irradiation growth, and plastic deformation of the cladding. VPSC has the ability to represent the mechanistic material processes controlling the deformation behavior of the cladding, such as dislocation glide and climb, dislocation-dislocation interactions, and dislocation vacancy/interstitial interactions within a framework that considers the crystallographic orientation of the grains within the matrix material. These capabilities far exceed the functionality of typical semi-empirical constitutive models employed in fuel behavior codes to model cladding deformation during irradiation. In addition, the VPSC framework provides a method to utilized information obtained from atomistic calculations that can expand or improve the formulations used to represent crystallographic deformation mechanisms.

The following summarizes the accomplishments achieved in the FY14 activities to incorporate the microstructurelly-aware, atomistically-informed, VPSC cladding mechanical constitutive model into the Peregrine engineering-scale fuel performance code. Advances were made in 1) developing an interface between VPSC and Peregrine that considers the computational and data requirements for each code, 2) the interface functionality was verified using a set of idealized cases and comparing the stand-alone VPSC version and the combined Peregrine-VPSC code, and 3) two demonstration cases were performed to highlight the impact of texture effects on irradiation growth modeling, and the importance of thermal creep activation energy on large deformation at high temperature.

5.1 Summary

The in-reactor deformation of zirconium alloy cladding is important to the safe and economic operation of nuclear reactors. The level of detail or fidelity required to simulate the mechanical deformation of a fuel rod depends on the knowledge of the material behavior under normal operation and accident conditions, and how the material behavior is modeled in the analysis methodology.

Traditional models used for the simulation of fuel elements are mostly based on empirical fitting of experimental data and the introduction of empirical parameters that have little or no connection with the actual physical mechanisms responsible for the mechanical behavior. As a consequence, their application is limited to the range of cladding tube microstructure, and temperature, dose and stress state conditions utilized for performing such fitting. Extrapolating these models to other conditions, such as abnormal operation or accident conditions, may not be justified and any calculations will have large uncertainty. As a consequence, there is a need to improve the predictive cladding capabilities with models that are based on physical material mechanisms and microstructure evolution during irradiation.

This report summarizes the results of implementing an approach that couples the engineering scale fuel performance code to material behavior models at the microstructure level to represent the constitutive law for mechanical deformations of zirconium alloy cladding.

The primary objective was to implement a polycrystal model for irradiation growth, irradiation creep, thermal creep and instantaneous plasticity based on crystallographic texture and microstructural defects into the engineering scale fuel performance code, Peregrine. Specifically, the Visco-Plastic Self-Consistent (VPSC) polycrystal code was adapted to account simultaneously for irradiation and thermal effects on zirconium alloy cladding deformation rate. Developing constitutive laws of creep and growth for cladding which explicitly incorporate the crystallographic mechanism of dislocation climb and glide, grain orientation, and interaction of grains with their surroundings constitutes a paradigm change in the way cladding mechanical behavior under irradiation is modeled today. There are several advantages to adopting such an approach. First, the directionality and anisotropy of the zirconium alloy cladding tube response is explicitly included in the model. As a result, deformation and stiffness can differ along each direction of the cladding tube because the model is based on tensor relations. There is no need to invoke 'effective stresses" or 'effective strain' scalar concepts. Second, the model uses information that is, in principle, accessible to measurements, such as distribution of grain orientation (texture) or dislocation density of mobile dislocations on different crystallographic planes (basal, prism, pyramidal) or density of irradiation induced dislocation loops. Third, a conceptual difference between a microstructurally-aware mechanistic constitutive model and empirical continuum laws for creep and growth is that the calculated mechanical deformations do not rely on an assumed superposition of deformation contributions (creep rate plus growth rate), but instead those mechanisms are coupled at the grain level and lead to a macroscopic response of cladding that is, in general, different from the sum of the individual mechanism contributions. As a matter of fact, irradiation growth, irradiation creep, thermal creep and instantaneous plasticity couple at the grain level as a consequence of grain interactions.

Interfacing the complex constitutive model of VPSC into a engineering scale finite element code is not a trivial task because: 1) a polycrystal is a assigned at each integration point to interrogate the constitutive response. As a consequence, it is necessary to track/update/store/transfer a large universe of internal variables for each grain that belongs to each polycrystal that is associated with each integration point; 2) the coupling of PEREGRINE and VPSC involves two nested iterative procedures: the outer one solves stress equilibrium conditions between elements in PEREGRINE, and the inner one provides a macroscopic response of the polycrystal that is consistent with the response of the individual constitutive response of the grains.

A numerical iteration method (Newton-Raphson method) to compute trial stress for given input of total strain was implemented to couple the VPSC module to Peregrine. A procedure of reducing the number of grains to provide representative crystallographic texture while reducing the computational time was developed. A number of benchmark cases have been run using Peregrine-VPSC, and results were compared to stand-alone VPSC results. The benchmark results demonstrate the successful functionality of the interface between Peregrine and the VPSC.

In addition, two cases were developed and executed to demonstrate the utility of using the mechanistic constitutive model from VPSC to calculate cladding deformation. First, irradiation growth calculations for set of cladding tube materials irradiated in power reactors was performed and comparison to a well-established empirical model is provided. Comparison of the empirical model and the VPSC model with reduced texture representation (two grains) demonstrated important differences between the microstructure model and the empirical correlation for the axial growth as a function material texture. The result suggest that the mechanism based microstructure model could provide more information which cannot be provided in the empirical modeling approach. The reduced number of grains in representing the crystallographic texture has provided an efficient method of running Peregrine-VPSC. The second case demonstrated the capability of modeling large deformation using Peregrine-VPSC, which is of interest to model the clad response under loss-of-

coolant accident conditions. Changes were required to the thermal creep activation energy used in VPSC to better represent the high temperature strain rate conditions. These results show that the localized clad thinning (or ballooning) under imposed axial temperature profile can be simulated by Peregrine-VPSC.

5.2 Future Work

The focus of the current Milestone was to develop physics-based constitutive models of cladding and to develop an interface with Peregrine which allows us to simulate fuel elements using this paradigm. The testing presented in Sections 3 and 4 demonstrates that this milestone has been reached. However, the testing has also identified some areas for further work in the microstructure physical models, the kinematic treatment, and the numerical procedures. Here we discuss areas that need improvement in order to implement a robust microstructurally-aware, atomistically-informed cladding constitutive model.

- Numerical efficiency and functionality

  Using reduced number of grains to represent crystallographic texture has resulted considerable reduction of the computation time for running Peregrine-VPSC. However, the current coupling of VPSC and Peregrine focuses mainly on its functionality and leaves plenty of room for code optimization. Increased numerical optimization could be achieved by: a) improving the numerical method, e.g., passing the Jacobian computed in VPSC to the MOOSE system to take advantage of the pre-conditioning method in the math library in the MOOSE code, b) eliminating VPSC calls at every iteration loop in Peregrine by keeping the polycrystal response 'frozen' until the load conditions at the integration point have changed enough; c) testing and enabling the parallel capability in the MOOSE for running large problem. All these improvements or refinements could boost the code's numerical capability in addition to the current method of reducing the number of grains represented in the model.

  The current results of running Peregrine-VPSC have demonstrated that the code is capable of providing more information than the traditional modeling approach, such as microstructure evolution in particular grain orientations, or stress fluctuations in grains which may be relevant to fracture processes. Further testing and adding functionalities in the code would be helpful to enhance the code's application.

- Material property benchmark

  The mechanism based microstructure deformation model depends on several parameters that require further definition over the range of materials. In the development of constitutive laws in VPSC, each individual deformation mechanism was benchmarked against measurement data reported in the literature. The loop nucleation rate versus dose was fit by Golubov et al (2011) to the experimental growth measured by Rogerson and Zee (1987) in single crystal zirconium at 553K. The irradiation creep is strongly coupled to growth because both share the same dislocation climb. Only one adjustable parameter is available, namely, the characteristic obstacle size that determines the climb distance of dislocations before they can glide. Here we identify it with the evolving loop radius, which is also a result of the growth model. In future developments we will have to contrast it to measured dimensional changes under irradiation, such as the ones reported by Butcher and Donohue (1986) for Zr-2.5%Nb mini-pressurized-tubes. A problem with irradiation creep is that it cannot be separated from the contribution of thermal creep.

  Thermal creep, on the other hand, can be measured in the absence of irradiation, and once adjusted, may be used for correcting experiments where irradiation and thermal contribute

simultaneously. For the current thermal creep law in VPSC the secondary creep data reported by Christodoulou et al (2002) for Zr-2.5%Nb, at different temperatures and load stress is used. We need to explore the implication on crystallographic mechanisms of the macroscopic thermal creep data reported by Wang et al (2013) for Zircaloy-4 at high temperature. Tensile test data reported by Le Saux et al (2008) in Zircaloy-4 non-irradiated and pre-irradiated, at different temperatures and rates is used for establishing the model parameters for instantaneous plasticity. Reactor applications will require further refinement of the material parameters for the domain of operating conditions and for the particular type of cladding alloy. In such case the best option is to make use of existing proprietary databases available to CASL and apply to them the mechanism fitting strategies developed during this Milestone. The next possible choice is to use empirical models which have been fit to specific data (such as axial deformation vs dose) as 'pseudo-experimental-data'. Material property benchmarking for high temperature would still be needed for modeling of accident conditions. Since the crystallographic texture representation and associated anisotropy is accounted for by the VPSC model, calibration of the model against multi-axial measurement data, if available, would help improve the reliability of the code.

- Improvement on the microstructure model

  Several simplifying assumptions concerning the crystallographic mechanisms are used here to derive the constitutive equations for irradiation growth (Eq 2-9), irradiation creep (Eq 2-11), thermal creep (Eq. 2-13) and instantaneous plasticity (Eq 2-15). In most cases the reason is that detailed experimental data at the micron scale is unavailable to justify more complex models. For example, TEM done by Griffiths (1988) in irradiated Zircaloy suggests that loops tend to nucleate at pyramidal dislocations, an observation that would favor loop formation in grains with a particular orientation. Research efforts on elucidating the atomistic mechanisms of loop nucleation and its dependence on alloying elements will be needed if we want to implement models based on such features. Another mechanism altering the balance of defect trapping, and so growth, are grain boundaries (Holt, 2008). The effects are likely to be relevant in small grain size cladding.

  Concerning thermal creep, insights on the mechanisms acting at high temperature is scarce and both, experimental information and diffusion models at the atomic scale, will be required to acquire better understand the dependence of activation energy Q with temperature. Q is a fundamental quantity in the VPSC crystallographic models and, as discussed in Section 4, the values fit at lower temperatures cannot be accurately extrapolated to higher temperatures. In what concerns instantaneous plasticity, the hardening law currently in VPSC (Eq. 2-18), depends on interaction parameters between glissile dislocations and between dislocations and irradiation loops. This is another example where a combination of careful experimental data, Dislocation Dynamics and atomistic simulations of dislocation-loop interaction can provide improved understanding on the strength of such interaction parameters.

  The positive message here is that the formalism described in this Milestone provides the right platform and the right length scale for implementing all of the above improvements and knowledge as they become available.

6. REFERENCE

R. B. Adamson, R. P. Tucker, and V. Fidleris, “High-Temperature Irradiation Growth in Zircaloy,” ASTM STP 754, 1982, pp. 208-234

A. Alankar, C.N. Tomé, R.A. Lebensohn, Multiscale material and component design with viscoplastic polycrystal models, Technical Report LA-UR-13-23909 Los Alamos National Laboratory (2013).

A. Arsenlis, B.D. Wirth, M. Rhee, (2004) Philosophical Magazine 84, 3617-3635

A. Arsenlis, M. Rhee, G. Hommes, R. Cook, and J. Marian, (2012) Acta Materialia 60, 3748-3757

J. Alvis and R. Montgomery, Licensing Criteria for Fuel Burnup Extension Beyond 62 GWd/tU: Industry Guide, EPRI, Palo Alto, CA: 2004. 1008108.

A.V. Barashev, S.I. Golubov, and R.E. Stoller, Theoretical investigation of microstructure evolution and deformation of zirconium under cascade damage conditions, Technical Report ORNL/TM-2012/225 Oak Ridge National Laboratory (2012)

I.J. Beyerlein and C.N. Tomé, “A dislocation based constitutive law for pure Zr including temperature effects”, Int J of Plasticity 24 (2008) 867-895

M. Billone, R. Montgomery, Y.R. Rashid, and J. Head, “Advancements in the behavioral modeling of fuel elements and related structures,” Nucl. Engrg. Des. 134, (1992), 23-36.

F.J. Butcher and S.A. Donohue, “In-reactor deformation of cold-drawn tubes of Zr-2.5 wt% Nb”, Internal report CNRL-4022 (1986)

B. Cazalis, J. Desquines (2007) Nuclear Technology 157, 215-229

N. Christodoulou, A.R. Causey, C.H. Woo, C.N. Tomé, R.J. Klassen, R.A. Holt, "Modeling the effect of texture and dislocation structure on irradiation creep of zirconium alloys", Proc. 16th Int. Symp. on "Effects of Radiation on Materials", ASTM STP 1175, A.S. Kumar, D.S. Gelles, R.K. Naustand and E.A. Little eds., American Society for Testing and Materials, Philadelphia (1994) 1111-28

N. Christodoulou, P.A. Turner, C.N. Tomé, C.K. Chow, R.J. Klassen, "Analysis of steady-state thermal creep of Zr-2.5%Nb pressure tube material", Metall. and Material Trans. 33A (2002) 1103-15

C. Deo, C. N. Tomé, R. Lebensohn, S. Maloy, (2008) J of Nuclear Materials 377, 136-140.

F. J. Erbacher, H.J. Neitzel, H. Rosinger, H. Schmidt, and K. Wiehr, “Burst Criterion of Zircaloy Fuel Claddings in a Loss-of-Coolant Accident,” ASTM 754, American Society for Testing and Materials, 1982, pp. 271-283

V. Fidleris, "The irradiation creep and growth phenomena", J Nuclear Mats 159 (1988) 22

D. G. Franklin, “Zircaloy-4 Cladding Deformation during Power Reactor Irradiation,” ASTM STP 754, American Society for Testing and Materials, 1982, pp.235-267

D. Gaston, C. Newman, G. Hansen, and D. Lebrun-Grandie´. MOOSE: A parallel computational framework for coupled systems of nonlinear equations. Nucl. Eng. Design, 239, p. 1768–1778, 2009.

K. Geelhoood, et. al., “FRAPCON-3.4: A Computer Code for the Calculation of Steady-State Thermal-Mechanical Behavior of Oxide Fuel Rods for High Burnup,” NUREG/CR-7022, Vol. 1, 2011

J.H. Gittus, (1974) Philosophical Magazine 30, 751-764

J.H. Gittus, "Theory of dislocation-creep due to the Frenkel defects or interstitialcies produced by bombardment with energetic particles", Phil Mag 25 (1972) 345-354

M. Griffiths, "A review of microstructure evolution in zirconium alloys during irradiation", J Nuclear Mats 190 (1988) 190-218

S.I. Golubov, A.V. Barashev, R.E. Stoller, B.N. Singh, "Breakthrough in understanding radiation growth in Zirconium", ASTM STP (2013), in press

S.I. Golubov, A.V. Barashev, R.E. Stoller, "On the origin of radiation growth in HCP crystals", ORNL/TM-2011/473 (2011)

M. N. Jahingir, J. Alvis, R. O. Montgomery, and O. Ozer, "Analysis of Fuel Behavior During LOCA Tests Using FALCON MOD01," Proceedings of the 2005 Water Reactor Fuel Performance Meeting, Kyoto, Japan, October 2-6, 2005

D. L. Hagrman et al., "MATPRO – Version 11 (Revision 2) A Handbook of Materials Properties for Use in the Analysis of Light Water Reactor Fuel Rod Behavior," NUREG/CR-0479, TREE-1280, Nuclear Regulatory Commission and EG&G (1981).

D. T. Hagrman, "MATPRO - A Library of Materials Properties for Light Water Reactor Accident Analysis," SCDAP/RELAP5/MOD3.1 Code Manual, Vol 4, NUREG/CR-6150, EGG-2720, June (1995).

R.A. Holt, "In-reactor deformation of Zirconium alloy components", J of ASTM Int, Vol 5 No. 6 (2008); also published in Proc. 15th Int Symp on Zirconium in the Nuclear Industry, ASTM STP 1505 (2009) 3-18

Heald PT and Harbottle JP, Journal of Nuclear Materials 67, p. 229 (1977)

N. E. Hoppe, "Engineering Model for Zircaloy Creep and Growth," Proceedings of the ANS-ENS International Topical Meeting on LWR Fuel Performance, p. 201-209, Avignon, France, April 21-24 (1991).

U.F. Kocks, C.N. Tomé, H.R. Wenk, "Texture and Anisotropy - Preferred Orientations in Polycrystals and their Effect on Materials Properties", Cambridge University Press (1998), 2nd edition (2000)

K. Lassmann, "The structure of fuel element codes," Nucl. Engrg. Des. 57 (1980) 17-39.

Lebensohn, R. and Tomé, C.N. (1993) Acta Metallurgica et Materialia 41, 2611-2624

Le Saux, M. L., Besson, J., Carassou, S., Poussard, C., Averty, X. (2008) J of Nuclear Materials 378, 60-69

M. Limbäck and T. Andersson, "A Model for Analysis of the Effect of Final Annealing on the In- and Out-of-Reactor Creep Behavior of Zircaloy Cladding," Zirconium in the Nuclear Industry: Eleventh International Symposium, ASTM STP 1295, p. 448-468, (1996).

W. Liu et al., "Numerical Method of Modeling Creep of Zirconium-alloy Cladding in a Multi-physics Fuel Performance Code," Proceedings of 2013 LWR Fuel Performance, Charlotte, NC, U.S.A., September 2013.

G. Lucas and R. Pelloux, (1981) Metallurgical Transactions A12, 1321-31

S. Maloy, M. James, G. Willcutt, W. Sommer, M. Sokolov, L. Snead, M. Hamilton, F. Garner, (2001) J of Nuclear Materials 296, 119-128

A. R. Massih, “An evaluation of high-temperature creep of zirconium alloys: data versus models,” Quantum Technologies AB Uppsala Science Park SE-751 83 Uppsala, Sweden Quantum Technologies Report: TR10-007v1.

Y. Matsuo, “Thermal Creep of Zircaloy-4 Cladding under Internal Pressure,” Journal of Nuclear Science and Technology, 24:2, p111-119, 1987.

R. O. Montgomery, “Analysis of Reactivity Initiated Accident-Simulation Tests Conducted at the CABRI and NSRR Facilities in France and Japan,” EPRI, Palo Alto, CA 2003. 1002863.

R. O. Montgomery, W. F. Lyon, M. N. Jahingir, and S. Yagnik, "Capabilities of the FALCON Steady State and Transient Fuel Performance Code", Proceedings of the 2004 International Meeting on LWR Fuel Performance, Orlando FL, September 19-22, 2004.

R. Montgomery, C. Stanek, W. Liu, and B. Kendrick, “US DOE CASL Program Fuel Performance Modeling for Steady State and Transient Analysis of LWR Fuel,”

R. O. Montgomery, “Peregrine: Advanced Modeling of Pellet-Cladding Interaction (PCI) Failure in LWRs,” Proceedings of the TopFuel 2012 Reactor Fuel Performance Meeting, Manchester, U.K., Sep. 2-6, (2012).

T. Onchi, H. Kayano, Y. Higashiguchi, (1977) J of Nuclear Science and Technology 14, 359-369

Y. Rashid, R. Dunham, and R. Montgomery, Fuel Analysis and Licensing Code: Falcon MOD01: Volume 1: Theoretical and Numerical Bases, EPRI, Palo Alto, CA: 2004. 1011307.

A. Rogerson and R.H. Zee, “High fluence irradiation growth in single crystal zirconium at 553K”, J. Nuclear Materials 151 (1987) 81-83

P.M. Sargent, M.F. Ashby, "Deformation maps for titanium and zirconium", Scripta Metall 16 (1982) 1415-22

J. Segurado, R. A. Lebensohn, J. LLorca, and C. N. Tomé, “Multiscale modeling of plasticity based on embedding the viscoplastic self-consistent formulation in implicit finite elements,” International Journal of Plasticity 28 (2012) 124–140.

Subramanian, G. and Tomé, C.N., Progress report on the incorporation of lower length scales into polycrystal plasticity model, Report LA UR 12-25612 (2012)

C. N. Tomé and R. A. Lebensohn, Visco-Plastic Self-Consistent (VPSC), ver. 7d, Los Alamos National Laboratory, Apr 1, 2012

P.A. Turner, C.N. Tomé, N. Christodoulou, C.H. Woo, "A self-consistent model for polycrystals undergoing simultaneous irradiation and thermal creep”, Philosophical Magazine A79 (1999) 2505-24

H. Wang, Z. Hu, W. Lu, M.D. Thouless, “A mechanism-based framework for the numerical analysis of creep in zircaloy-4”, J Nuclear Mats 433 (2013) 188-198

R. Williamson, J. Hales, S. Novascone, M. Tonks, D. Gaston, C. Permann, D. Andrs, and R. Martineau, “Multidimensional multiphysics simulation of nuclear fuel behavior,” Journal of Nuclear Materials 423(2012) 149-163.

C.H. Woo, J of Nuclear Materials 131 (1985) 105

7. APPENDIX

Table A-1 Elongation data from characterized fuel rods (Franklin, 1982)

Vendor	Type	Number of rods[a]	Fluence X10^{-21} n/cm^2 E> 1MeV	Cos(θ_{max})	Yield Stress (MPa)	Hoop stress (MPa)	$\Delta L/L$
CE	SSM	4	3.07	0.857	497.6	79.82	0.00315
CE	SSM	8	4.28	0.857	497.6	79.82	0.00414
CE	SSM	4	3.06	0.857	497.6	114.27	0.0044
CE	SSM	8	4.28	0.857	497.6	97.05	0.00503
CE	SSM	8	3.97	0.857	497.6	79.82	0.00435
CE	SSM	3	3.05	0.857	497.6	97.05	0.00409
CE	SSM	3	3.86	0.857	497.6	79.82	0.00523
CE	SSM	3	3.85	0.857	497.6	97.05	0.00556
CE	SSM	15	4.16	0.857	497.6	79.82	0.00435
W	W	24	6.72	0.766	612.1	76.77	0.0067
W	W	7	2.88	0.766	612.1	76.77	0.00332
W	W	28	5.11	0.766	612.1	76.77	0.00532
W	W	6	1.61	0.766	612.1	76.77	0.00173

[a] Average value of irradiation growth ($\Delta L/L$) was reported when multiple rods were measured

Table A-2 Elongation data from characterized non-fueled rods (Franklin, 1982)

Vendor[a]	Type	Number of rods	Fluence X10^{-21} n/cm^2 E> 1MeV	Cos(θ_{max})	Yield Stress (MPa)	Hoop stress (MPa)	$\Delta L/L$
CE	SSM	1	3	0.8746	497.6	131.5	0.00413
CE	SSM	1	4.19	0.8746	497.6	131.5	0.00591
CE	SSM	1	3.04	0.8746	497.6	97	0.00351
CE	SSM	1	4.21	0.8746	497.6	97	0.00474
CE	SSM	1	4.19	0.8746	497.6	79.8	0.00466
CE	SSM	1	4.21	0.8746	497.6	79.8	0.00371
CE	WOLV	1	3.05	0.848	440	131.5	0.00368
CE	WOLV	1	4.29	0.848	440	97	0.0038
CE	WOLV	1	4.18	0.848	440	79.8	0.00347
CE	Zirt	1	3.02	0.6427	467.2	131.5	0.00181
CE	Zirt	1	4.18	0.6427	467.2	131.5	0.00281
CE	Zirt	1	4.29	0.6427	467.2	131.5	0.00299

[a] The B&W rods were not individually characterized for length and were not included.